Research Article: Methods/New Tools | Novel Tools and Methods

Information theoretic approaches to deciphering the neural code with functional fluorescence imaging

1 **Manuscript Title Page**

2 **1. Manuscript Title (50 word maximum)**

3

4 Information theoretic approaches to deciphering the neural code with functional fluorescence imaging

5 **2. Abbreviated Title (50 character maximum)**

6

7 Information metrics for functional fluorescence imaging

8 **3. List all Author Names and Affiliations in order as they would appear in the published article**

9 Jason R. Climer[1], PhD and Daniel A. Dombeck[1]*, Ph.D.

10 [1] Department of Neurobiology, Northwestern University, Evanston IL

11 **4. Author Contributions:** Each author must be identified with at least one of the following:

12 JRC and DAD Designed research, JRC Performed research, JRC Analyzed data, JRC and DAD Wrote the
13 paper.

14 **5. Correspondence should be addressed to (include email address)**
15 *Correspondence: d-dombeck@northwestern.edu

16
17

18 **6. Number of Figures (5**
19 **main, 9 extended**
20 **data)**
21 **7. Number of Tables (0)**
22 **8. Number of**
23 **Multimedia (0)**
24

25 **9. Number of words for Abstract (148)**
26 **10. Number of words for**
27 **SignificanceStatement (113)**
28 **11. Number of words for Introduction (2004)**
29 **12. Number of words for Discussion** (1410
30

31 **13. Acknowledgements**

32

38 **14. Conflict of Interest**

39
40 Authors report no conflict of interest

41 **15. Funding sources**

Information theoretic approaches to deciphering the neural code with functional fluorescence imaging

Abstract

Information theoretic metrics have proven useful in quantifying the relationship between behaviorally relevant parameters and neuronal activity with relatively few assumptions. However, these metrics are typically applied to action potential recordings and were not designed for the slow timescales and variable amplitudes typical of functional fluorescence recordings (e.g. calcium imaging). The lack of research guidelines on how to apply and interpret these metrics with fluorescence traces means the neuroscience community has yet to realize the power of information theoretic metrics. Here, we used computational methods to create mock action potential traces with known amounts of information. From these, we generated fluorescence traces and examined the ability of different information metrics to recover the known information values. We provide guidelines for how to use information metrics when applying them to functional fluorescence and demonstrate their appropriate application to GCaMP6f population recordings from mouse hippocampal neurons imaged during virtual navigation.

Significance Statement

Functional fluorescence imaging and information theoretic quantification could provide a powerful new combination of tools to study neural correlates of behavior, but functional fluorescence signals represent altered versions of the underlying physiological events. Therefore, it is unclear if or how information metrics can be applied to functional fluorescence imaging data. Here, we performed an in-depth simulation study to examine the application of the widely used bits per second and bits per action potential metrics of mutual information to functional florescence recordings. We provide guidelines for how to use information metrics when applying them to functional fluorescence and demonstrate their appropriate application to GCaMP6f population recordings from mouse hippocampal neurons imaged during virtual navigation.

Introduction

Neurons encode parameters important for animal behavior, at least in part, through the rate of production of action potentials (APs). Evidence for this can be found from electrophysiological AP recordings of orientation tuning in the visual system (Hubel and Wiesel, 2009), chemical sensing in the olfactory system (Leveteau and MacLeod, 1966; Wachowiak and Shipley, 2006), and spatial encoding in the hippocampus (O'Keefe, 1976). Key to deciphering the neural code, therefore, is defining metric to quantify the relationship between behavioral parameter spaces and a neuron's spiking rate. There are many metrics used for quantification, and are often used to compare neural responses across conditions or in neurons with complex responses. The underlying assumptions of the different metrics then become important factors to consider when determining which one to use.

Information theory is growing in popularity in the neuroscience community, largely because it provides a means to quantify rate coding with relatively few assumptions. One useful information theoretic measure is mutual information (MI), which is typically measured in bits per unit time, and describes the increase in predictability of the neural response when behavioral parameters are known. Formally, mutual information is the information about one variable that can be extracted from another, such as the information about behavior that can be derived from observing neural activity. Mutual information can be applied to neurons with widely varying response properties because it:

1. Is a nonlinear metric, not requiring the linearity assumptions of correlation metrics (e.g. (Grubb and Thompson, 2006; Hinman et al., 2016; Jiaying Tang, 2015; Kropff et al., 2015),
2. Does not assume a response shape, as is typical with Gaussian field mapping metrics (e.g. Kraus et al., 2015; Soo et al., 2011) or metrics using exponential or polynomial curve fitting (Hinman et al., 2016; Jiaying Tang, 2015), and
3. Uses the full time trace or shape of the mean response profile, rather than defining receptive fields with thresholding (e.g. Harvey et al., 2009; Niell and Stryker, 2008; Pastalkova et al., 2008).

However, MI can be nontrivial to estimate from neural and behavioral recordings and its estimation is an ongoing area of research (Belghazi et al., 2018; Gao et al., 2017; Kraskov et al., 2004; Timme and Lapish, 2018).

Here we focus on the most widely used estimator of MI in neuroscience, the SMGM estimator developed by Skaggs, McNaughton, Gothard and Markus (Skaggs et al., 1993), though as a point of comparison, we also consider the Binned Estimator (Timme and Lapish, 2018) and a separate technique developed by Kraskov, Stogbauer and Grassberger (KSG, Kraskov et al., 2004). The Binned Estimator estimates the joint probability distribution using a 2D histogram of neural response vs. behavioral variable; this transforms continuous variables into discrete values (Timme and Lapish, 2018). KSG estimates mutual information by examining the distance between data-points in the neural activity-behavioral parameter space. The SMGM estimator, on the other hand, relies on the assumption that AP firing follows an inhomogeneous Poisson process. The SMGM estimator therefore requires binning of only the behavioral variable(s), in contrast to the Binned Estimator. The profile of firing rates vs. behavioral variable is then used to estimate the MI.

The relative simplicity of the SMGM estimator has added to its popularity and widespread use in neuroscience applications for estimating behavioral information contained in single unit AP recordings. This metric has proven useful in quantifying rate coding in place cells (Knierim et al., 1995; Lee et al., 2006; Markus et al., 1995; Poucet and Sargolini, 2013), complex spatial responses of hippocampal interneurons (Frank et al., 2001; Wilent and Nitz, 2007), odor sequence cells (Allen et al., 2016), time cells (MacDonald et al., 2013), head direction cells (Stackman and Taube, 1998), speed cells (Fyhn et al., 2002), and face differential neurons (Nguyen et al., 2014, 2013), and has been used across multiple

116   different species (Hazama and Tamura, 2019; Mankin et al., 2019; Yartsev and Ulanovsky, 2013).
117   Furthermore, as a single neuron metric it provides statistical power for comparisons. Thus, it has been
118   used to quantify differences in rate coding across different brain regions (Simonnet and Brecht, 2019)
119   and across experimental interventions such as lesions (Calton et al., 2003; Liu et al., 2004), inactivations
120   (Brandon et al., 2011; Hok et al., 2013; Huang et al., 2009; Koenig et al., 2011), and applications of
121   drugs (Newman et al., 2014; Robbe and Buzsáki, 2009). Further, it has been used to examine differences
122   in encoding across different behaviors (Aronov and Tank, 2014; Park et al., 2011; Zinyuk, 2000), and
123   disease states (Fu et al., 2017; Gerrard et al., 2008; Zhou et al., 2007). SMGM information is often
124   normalized from measuring bits per unit time to instead measure bits per AP. This creates a measure
125   sensitive only to the selectivity of a neuron, and not its average firing rate. Thus, SMGM is a powerful
126   tool for measuring the neural code in electrophysiological recordings of APs.

127   The power of MI estimators has yet to be fully exploited by the neuroscience community. For example,
128   the estimators have not yet been widely used to compare encoding properties of large numbers of
129   genetically identified neurons, or to quantify information content of other discrete signaling events such
130   as synaptic inputs; both of which are difficult to study using electrophysiological methods. *In vivo*
131   imaging of functional indicators has emerged as an important tool, largely because it possesses these
132   capabilities. For example, using fluorescent calcium indicators, the functional properties of large
133   populations of neurons can be simultaneously recorded in rodents (Dombeck et al., 2007; Radvansky
134   and Dombeck, 2018; Sheffield et al., 2017; Stirman et al., 2016; Stringer et al., 2019; Ziv et al., 2013)
135   zebrafish (Ahrens et al., 2013), or invertebrates such as *C. elegans* (Nguyen et al., 2016) and *Drosophila*
136   (Keller and Ahrens, 2015; Mann et al., 2017). Furthermore, *in vivo* imaging can assure the genetic
137   identity of the recorded neurons (Jing et al., 2018a, 2018b, 2018c; Khoshkhoo et al., 2017; Sheffield et
138   al., 2017) and can access subcellular structures, allowing for functional recordings from synapses and
139   dendrites using different functional fluorescent indicators (e.g. Jing et al., 2018d; Marvin et al., 2019,
140   2018; Scholl et al., 2017; Sheffield et al., 2017; Sheffield and Dombeck, 2015).

141   However, these indicators generate signals that are different from the underlying quantal events. For
142   example, somatic calcium indicators reveal intensity variations that are correlated with somatic AP
143   firing rates but are a smoothed and varying amplitude version of the AP train. This transformation from
144   AP train to fluorescence trace is an active area of research (Dana et al., 2018; Éltes et al., 2019;
145   Greenberg et al., 2018), but it is often approximated by convolving the AP train with a kernel, which
146   defines the indicator's response to a single AP. The shape of the kernel is a function of the indicator
147   expression level, intracellular calcium buffering, amount of calcium influx, efflux rates, background
148   fluorescence, resting calcium concentration, and other factors. When measured in pyramidal neurons,
149   average kernels typically take the shape of a sharp increase in fluorescence followed by an exponential
150   decay to baseline (Chen et al., 2013; Dana et al., 2018; Pachitariu et al., 2018; Park et al., 2013; Yaksi
151   and Friedrich, 2006). Therefore, while functional fluorescence imaging and information theoretic
152   quantification may prove to be a powerful new combination of tools to study neural correlates of

4

153 behavior, it is critical to remember that functional fluorescence signals represent altered versions of the
154 underlying physiological events.

155 Caution is then needed when applying information metrics to continuous functional fluorescence traces,
156 yet the imaging community is already beginning to use information metrics, particularly SMGM. This
157 metric has been applied to somatic calcium responses to compare the information content of the same
158 neurons across different behavioral epochs (Heys and Dombeck, 2018), across different populations of
159 neurons in different brain regions (Hainmueller and Bartos, 2018), across different genetically identified
160 neural populations (Khoshkhoo et al., 2017), or to examine encoding by subcellular structures (Rashid et
161 al., 2020), or to classify the significance of encoding particular parameters by individual neurons
162 (Kinsky et al., 2018; Mau et al., 2018; Rashid et al., 2020).

163 However, it is essential to recognize some of the assumptions underlying these information metrics are
164 violated by functional florescence recordings. All three metrics (SMGM, KSG and Binned Estimation)
165 assume stationarity in the neural response, which is violated by the elongated time responses and
166 relatively slow fluctuations of the fluorescence intensity of the reporters. When applied to spiking data,
167 there is also a change in units: rather than AP counts, functional fluorescence traces are typically plotted
168 in units of florescence change with respect to baseline ($\Delta F/F$). One possible solution to these issues
169 would be to deconvolve calcium traces to recover APs; however, deconvolution is an active area of
170 research, and the accuracy of these methods has recently been questioned (Evans et al., 2019). Ideally,
171 the calcium traces could be used directly to measure spiking information, without the need for such an in
172 between, potentially error inducing, step.

173 Quantifying the effects of the above violations on measurements of information using functional
174 fluorescence recordings with an analytical solution is particularly challenging with behaviorally
175 modulated neural recording data. However, a more tractable means of quantifying the effects would be
176 to use a simulation study to measure the induced biases and changes in measurement quality (Morris et
177 al., 2019). This strategy makes use of pseudo-randomly generated AP traces and has the advantage that
178 the ground truth parameters of the simulations are known, while variability due to behavior and other
179 features can be incorporated (Climer et al., 2015, 2013; Cohen and Kohn, 2011; Østergaard et al., 2018).

180 To provide the field with guidelines for the use of information metrics applied to functional fluorescence
181 recording data, we used computational simulation methods to create a library of ten thousand mock
182 neurons whose spiking output carry an exact, known (ground-truth) amount of information about the
183 animal's spatial location in its environment. We used real behavioral data (available at
184 https://doi.org/10.7910/DVN/SCQYKR) of spatial position over time from mice navigating in virtual
185 linear tracks and then simulated the spatial firing patterns of the mock neurons using an inhomogeneous
186 Poisson process framework (Brown et al., 2003; Climer et al., 2013; Paninski, 2004). We then simulated
187 fluorescent calcium responses for each neuron in each session by convolving the AP trains with calcium
188 kernels for different indicators, primarily GCamp6f (Chen et al., 2013), and then we added noise. MI

5

189 metrics (between spatial location and the neural signals) were then applied to the spiking or fluorescence
190 traces to quantify the performance of the metrics for estimating information. We provide a user toolbox
191 (found at https://github.com/DombeckLab/infoTheory), which consists of Matlab functions to generate
192 libraries of model neurons with known amounts of information, to generate spiking or fluorescence
193 time-series from those model neurons, and to estimate neuron information from real or model spiking or
194 fluorescence time-series datasets using the three metrics considered here (SMGM, Binned Estimator,
195 KSG). We focused on testing the performance of the SMGM method, and then compared its
196 performance to the Binned Estimation and KSG methods, which do not have the underlying Poisson
197 assumption required for the SMGM approach. We also applied a deconvolution algorithm to test its
198 performance. We then applied this analysis to real datasets of hippocampal neuron populations from
199 mice navigating in virtual linear tracks. We quantified the spatial information content of the populations
200 and then performed Bayesian decoding of mouse position from different information containing subsets
201 of this population. Interestingly, we found that the population quantile with the lowest information
202 values were still able to decode mouse position to the closest quarter of the track. Thus, we provide new
203 findings about the neural code for space that were made possible by the information metrics and
204 guidelines that we introduce here.

205 The SMGM method applied directly to the mean ΔF/F intensity map appeared to best recover the
206 ground truth information. We provide guidelines for the use of the SMGM metric when applied to
207 functional fluorescence recordings and demonstrate the appropriate application of these guidelines to
208 GCaMP6f population recordings from hippocampal neurons in mice navigating virtual linear tracks.

Materials and Methods

209
210 *Toolbox and Data Availability*
211 We provide a user toolbox (freely available at https://github.com/DombeckLab/infoTheory), which
212 consists of Matlab functions to generate libraries of model neurons with known amounts of information,
213 to generate spiking or fluorescence time-series from those model neurons, and to estimate neuron
214 information from real or model spiking or fluorescence time-series datasets using the three metrics
215 considered here (SMGM, Binned Estimator, KSG). This toolbox also contains tools to generate mock
216 neurons using a binned distribution, avoiding the Poisson assumption of SMGM. Behavioral data used
217 to generate the random traces is freely available at https://doi.org/10.7910/DVN/SCQYKR.

218 *Construction of AP trains with known ground truth information*
219 To construct mock neurons with ground truth information, we adapted the differential form of the AP
220 information, in bits per AP (Equation 6). To create a rate map, we first selected an average firing rate
221 and target ground truth information. The mean rate ($\bar{\lambda}$) was always between 0.1 and 30 Hz, the
222 information in bits per AP (I_{AP}^{E}) between 0 and 6 bits per AP, and the information in bits per second (I_{s}^{E})
223 between 0 and 24. To more evenly sample each of these, we first randomly selected the bits per second
224 (I_{s}^{E}) or bits per AP (I_{AP}^{E}) to target. If the information target was in bits per AP, both the information (I_{AP}^{E})

6

225   and mean firing rate ($\bar{\lambda}$) were chosen uniformly. Because the information in bits per second $I_S^E = \bar{\lambda} I_{AP}^E$,
226   the bits per second information was not uniformly sampled in this case. If the target was to be in bits per
227   second, both the bits per AP (I_{AP}^E) and SMGM bits per second (I_s^E) measures were first chosen
228   uniformly. Because the rate $\bar{\lambda} = I_S^E / I_{AP}^E$, this was not chosen uniformly. This procedure was repeated to
229   maintain the bounds on $\bar{\lambda}$, resulting in a non-uniform sampling of information. The final distribution
230   (Figure 1C) was spread acceptably for further analysis.

231   The rate maps were constructed by spline interpolating across 5 control points with two anchored at each
232   end of the track, and taking the exponential for each point, and then normalizing by the numerically
233   calculated integral (Figure 1A, D). To create a map matching the target information, we began with a
234   random spline. The 'y' (relative rate) initial position of each node was chosen from a standard normal
235   distribution and the initial 'x' (track position) of the 3 center nodes was chosen uniformly. The nodes
236   were then systematically moved using the MATLAB built in optimizer 'fmincon' with constraints
237   preventing the crossing of the center nodes and keeping them on the track, and the
238   'OptimalityTolerance' option set to 0 (Figure 1A). This was accomplished using the 'genExpSpline'
239   function' in the toolbox.

240   We then randomly selected behavioral traces (see Methods *Behavior* section) and concatenated sessions
241   until a total time randomly chosen between 3 and 60 minutes was reached (Figure 1E, F; Figure 2A,
242   Figure 3A). This was accomplished using the 'loadBehaviorT' function in the toolbox. The track
243   positions were normalized and used to build a conditional intensity function (CIF) from the rate function
244   above. The CIF was normalized to match an expected mean rate over the entire session, and the
245   MATLAB built-in 'poissrnd' function was used to generate AP times, sampled at 1 kHz. The was
246   accomplished using the 'genSpikeTrain' function in the toolbox. Finally, the AP times were binned
247   according to the counts within mock imaging frames sampled at 30 Hz.

248   *Simulated $\frac{\Delta F}{F}$ traces*

249   To construct the $\frac{\Delta F}{F}$ traces (Figure1E,J,K; Figure2A; Figure3A), we first created a single AP response
250   kernel from the peak-normalized sum of two exponentials:

$$g(t) = \frac{e^{-at} - e^{-bt}}{\left(\frac{a}{b}\right)^{\frac{a}{b-a}} - \left(\frac{a}{b}\right)^{\frac{b}{b-a}}}$$

7

251 Where t is the time since the AP and a and b are chosen to minimize $\left(1 - g(\tau_{rise})\right)^2 + \left(0.5 - \right.$

252 $\left. g\left(\tau_{rise} + \tau_{fall}\right)\right)^2$ where τ_{rise} is the rise time in seconds and τ_{fall} is the half-fall time in seconds.

253 Deviations in τ_{rise} and τ_{fall} from baseline were also measured. The kernel g(t) was then multiplied by

254 the indicator height. The kernel parameters were generated using the 'fluorescenceKernel' function, and

255 evaluated using the 'doubleExp' function in the toolbox.

256 The GCaMP6f, GCaMP6s, and jRGECO1a heights, rise and fall times were measured as responses to

257 single APs *in vivo* (Chen et al., 2013; Dana et al., 2019)*:* other kernels (Figure 2H, Figures 2-2 and 3-1)

258 were approximated from other experiments presented in the references (seen in Table 1).

259 *Table 1. Properties of indicator kernels used*

Kernel	Height $\Delta F/F$	Rise (s)	Fall (s)	Source
gCaMP6f	0.190	0.042	0.142	(Chen et al., 2013)
jRGECO1a	0.164	0.041	0.207	(Kalko et al., 2011)
gCaMP7f	0.560	0.063	0.276	(Dana et al., 2019)
gCaMP6s	0.230	0.179	0.550	(Chen et al., 2013)
iGluSnfR-A184S	0.300	0.022	0.106	(Marvin et al., 2018)

260

261 To define the width of the kernel (Figure2L-N, Figure3K-M), we considered the kernel as a low pass

262 filtered version of the APs. If we normalize the filter to mean 1, it has the Fourier transform $\left(\frac{1}{a+2\pi f j} - \right.$

263 $\left. \frac{1}{b+2\pi f j}\right)\left(\frac{ab}{b-a}\right)$. The kernel width was defined as the -3 dB (50%) cutoff period of this filter: $f^{-1} =$

264 $\frac{\sqrt{-a^2-b^2+\sqrt{a^4+14a^2b^2+b^4}}}{2\pi\sqrt{2}}$. For the simulations with different width kernels, a kernel width was chosen

265 between 0.01 and 10 seconds, a rise time between 0.001 and 1 second, and a fall time between the rise

266 time and 2 seconds. Then, a and b were chosen to minimize the squared error between these three targets

267 using the built in MATLAB optimizer 'fminsearch'.

268 White noise with a standard deviation of $0.15 \frac{\Delta F}{F}$ was then added to the mock fluorescence traces.

269 *Nonlinearity*

270 In our linear simulations used throughout this work, the fluorescence kernels associated with a fast

271 sequence of action potentials were approximated to sum linearly. In real cultured neurons, a summation

272 nonlinearity has been observed such that sequences of action potentials do not generate a linear

8

273 summation in ΔF/F (Dana et al., 2019). To simulate this nonlinearity, the $\frac{\Delta F}{F}$ trace was then further
274 transformed as:

$$\frac{\Delta F'}{F} = sign\left(\frac{\Delta F}{F}\right) * \frac{6.264}{1 + e^{-3.251\, Re\left(\log_{10}\left(\frac{\Delta F}{F}\right)\right)}}$$

275 This equation was arrived at by fitting the measured responses in Dana et al, 2019, Figure 2C, which
276 can be compared to the nonlinearity used here (Figure 3-3A).

277 *Deconvolution*
278 Deconvolution was performed using the previously described FOOPSI algorithm (Friedrich et al., 2017;
279 Vogelstein et al., 2010). The regularization coefficient was set at 0.02154, which maximized the
280 correlation between the deconvolved trace and the true spike train in a random sample of 500 simulated
281 traces: all other parameters were optimized for each trace. Because the example regularization
282 coefficient provided by Friedrich et al, 2017 was 2.4, we also measured information values at 100
283 different values for the regularization coefficient between 0 and 3; this had little effect on the measured
284 information (Figure 4-1).

285 *KSG estimator*
286 The previously described second KSG estimator (Kraskov et al., 2004) was used using the 5th nearest
287 neighbor distance.

288 *Binned estimators*
289 The binned mutual information estimators were used (Timme and Lapish, 2018). The activity trace was
290 divided into 10 bins, either evenly across the span of the activity (uniform binned) or variably so the
291 bins contained the same number of samples (occupancy binned). Position was similarly divided into 60
292 bins.

293 *Gaussian simulations*

294 To compare the analytic approximation to our numerical method, the numerical techniques had to be
295 applied to place cells with Gaussian rate maps. The same target information, firing rates, and behavior
296 were used as for our original 10,000 simulations with spline rate maps. However, instead the rate map
297 was chosen as a Gaussian with width $\sigma = e^{\frac{1}{2}\left(-1 - 2I_{AP}^{E} \log(2) - \log(2\pi)\right)}$. For the numeric simulations, the
298 true amount of information was calculated using a numeric integrator. The instantaneous rate was
299 calculated using the normal distribution PDF. This was normalized and used to generate a spike train
300 and florescence trace as above.

9

301 *Bayesian decoding*
302 The Bayesian decoder used here (Figure 5 G,H) was adapted from a previously described method
303 (Zhang et al., 1998). Decoding was performed on the likelihood that a significant transient occurred in a
304 time frame, trained on the first 80% of the session and tested on the last 20%. The session was divided
305 into Δt=0.1 second bins. The conditional likelihood that an animal is in position x_i given the number of
306 active frames during a time window (n) is $p(x_i|n) = p_X(x_i)\left(\prod_{j=1}^{M} f_{i,j}^{n_j}\right) e^{-\Delta t \sum_{j=1}^{M} f_{i,j}}$, Where $p_X(x_i)$ is
307 the (marginal) probability that the animal is in the ith spatial bin during a time sample, $f_{i,j}$ is the average
308 rate of significant frames by the jth neuron in the ith spatial bin, n_j is the number of significant frames
309 observed during the time window in neuron j, and M is the total number of neurons. The decoded
310 position was selected as the one with maximum conditional likelihood.

311 *Animals*
312 10 to 12 week old male C57BL/6 mice (20-30g) were individually housed under a reverse 12 hr. light /
313 dark cycle, all experiments were conducted during the dark phase. All experiments were approved by
314 the Northwestern University Animal Care and Use committee.

315 *Behavior*
316 We used a previously described virtual reality set-up and task (Heys et al., 2014; Sheffield et al., 2017;
317 Sheffield and Dombeck, 2015); some of the behavior sessions used here has previously appeared in
318 these studies. Briefly, water scheduled, head fixed mice were trained to run on a cylindrical treadmill
319 down a 3m virtual track to receive a water (4 ul) reward at the end of the track, and were subsequently
320 teleported to the beginning of the track after a 1.5 s delay. Behavioral sessions were included if the
321 animal ran at least 20 laps containing a continuous 40 cm run for which the velocity was over 7 cm/sec
322 during a 5-30 minute session.

323 *Mouse surgery and virus injected*
324 We performed population calcium imaging of CA1 neurons as described previously (Sheffield et al.,
325 2017; Sheffield and Dombeck, 2015). Briefly, 30 nL of AAV1-SynFCaMP6f (University of
326 Pennsylvania Vector Core, 1.5*10^13 GC/ml) was injected through a small craniotomy over the right
327 hippocampus (1.8 mm lateral, 2.3 mm caudal of Bregma; 1.25 mm below the surface of the brain) under
328 Isoflurane (1-2%) anesthesia. 7 days later, a hippocampal window and head plate was implanted as
329 described previously (Dombeck et al., 2010).

330 *Two-photon imaging*
331 Imaging was performed as previously described (Sheffield et al., 2017; Sheffield and Dombeck, 2015).
332 Scanimage 4 was used for microscope control and acquisition (Pologruto et al., 2003). Time series
333 movies (1024 or 512x256 pixels) were acquired at 50 Hz. A Digidata1440A (Molecular Devices) with
334 Clampex 10.3 synchronized position on the linear track, reward timing, and the timing of image frames.

10

Image processing, ROI selection and calcium transient analysis
Images were processed as previously described (Sheffield et al., 2017; Sheffield and Dombeck, 2015), with minor modifications. Briefly, rigid motion correction was performed using cross correlation as in (Dombeck et al., 2010; Miri et al., 2011; Sheffield and Dombeck, 2015), but here using a Fast-Fourier transform approximation on the full video. ROIs were defined as previously described (Mukamel et al., 2009) (mu=0.6, 150 principal/independent components, s.d. threshold = 2.5, s.d. smoothing width=1, area limits = 100-1200 pixels). $\frac{\Delta F}{F}$ traces were generated by normalizing around the 8th percentile of a 3 second sliding window. Significant transients from both experimental and mock fluorescence traces were selected by comparing the ratio of amplitudes and durations of positive to negative going transients with a false positive rate <0.01% (Dombeck et al., 2010). Mock traces used the histograms generated from the mock gCaMP6f traces (Figure 2-3) or from the specific matching indicator traces (Figures 2-2 and 3-1): experimental data histograms were built separately. All subsequent analyses were run using these significant transients.

Behavior analysis
The mean virtual track velocity was defined as the total virtual track distance covered during the session divided by the total duration of the session; slow and stop periods were included in this metric. All other analyses were restricted to long running periods, where the animal exceeded a virtual track velocity of 4 cm/s and ran continuously for at least 40 cm.

Defining place fields
Place fields were defined by first creating the spatial fluorescence intensity map (f_i) with the 300 cm track divided into 60, 5 cm bins. This map was smoothed via a 3 bin boxcar. Transients identified during run periods were shuffled in order and to random intervals to create 1000 bootstrapped intensity maps. Candidate fields were defined as regions of the original fluorescence map with values greater than 99% of the bootstrapped maps. Fields were then retained if they were between 20 and 120 cm wide: significant place cells retained at least one field that satisfied these criteria.

Results

The SMGM information metrics
Here we review the derivation of the SMGM information metrics and the underlying assumptions. For illustrative purposes throughout this manuscript, we use the example of spatial encoding in which the firing pattern of neurons carry information about the animal's location along a linear track; however, the derivations, equations and conclusions generalize to encoded variables over other domains and dimensionalities.

Consider a random variable X representing the positions an animal might take, with x being its value measured at one time sample. The positions are subdivided into N spatial bins, such that x can take on the values $\{1, 2, ..., N\}$. For our analyses, N=60. Consider a random variable Y representing the number

11

370 of APs a neuron might fire, where y is the count measured within a time sample. y can take on the
371 values of $\{0, 1, \ldots, +\infty\}$. X and Y are both discrete. If X and Y both obey the assumption that each time
372 sample is independent (i.e. they are stationary), then the mutual information (I, in bits per sample)
373 between X and Y is expressed as follows:

$$I(X; Y) = \sum_{i=1}^{N} \sum_{y=0}^{+\infty} p_{X,Y}(x_i, y) \log_2 \frac{p_{X,Y}(x_i, y)}{p_X(x_i) p_Y(y)} \qquad \qquad 1$$

374

375 Where $p_X(x_i)$ is the (marginal) probability that the animal is in the ith spatial bin during a time sample,
376 $p_Y(y)$ is the probability that the neuron fires y APs in the time sample, and $p_{X,Y}(x_i, y)$ is the joint
377 probability that the neuron fires y APs and is in the ith bin. Recall that $p_{X,Y}(x_i, y) = p_{Y|X}(y|x_i) p_X(x_i)$,
378 where $p_{Y|X}(y|x_i)$ is the conditional probability that the neuron fires y APs given that the animal is in the
379 i^{th} spatial bin. We can thus rewrite Equation 1 as follows:

$$I(X; Y) = \sum_{i=1}^{N} \sum_{y=0}^{+\infty} p_{Y|X}(y|x_i) p_X(x_i) \log_2 \frac{p_{Y|X}(y|x_i)}{p_Y(y)} \qquad \qquad 2$$

380 With the further assumption that the firing of the neuron follows Poisson statistics, we can then estimate
381 the mutual information as follows: let the AP rate (AP/s or Hz) in a single bin be λ_i, and the average
382 across the session be $\bar{\lambda}$. For an arbitrarily small time window Δt, the probability that an AP occurs in
383 that window is $\Pr(Y = 1 | x = i) = \lambda_i \Delta t$, with the probability that an AP occurs regardless of position as
384 $\Pr(Y = 1) = \bar{\lambda} \Delta t$. We can thus rewrite Equation 2 as:

$$I(X; Y) = \sum_{i=1}^{N} \lambda_i \Delta t\, p_X(x_i) \log_2 \frac{\lambda_i}{\bar{\lambda}} \qquad \qquad 3$$

385 By integrating over one second ($\int_0^1 I(X; Y) d\Delta t$) we obtain the first key SMGM metric for spatial
386 information as measured by AP firing, which is in units of bits per second:

$$\widehat{I_s^E} = \sum_{i=1}^{N} \lambda_i p_X(x_i) \log_2 \frac{\lambda_i}{\bar{\lambda}} \qquad \qquad 4$$

387 For notation, we will use a carrot (^) to indicate an information value that is measured from experiment,
388 the superscript (E in this case) to show the source of the data, and a subscript to show the units/formula

389 used (bits per second in this case). Thus, $\widehat{I_s^E}$ is the information measured via electrophysiology in bits per
390 second. This metric is linearly dependent on the average firing rate of the neuron, and this dependence is
391 often removed through normalization by the average firing rate to obtain the second key metric of spatial
392 information as measured by AP firing, which is in units of bits/(second*Hz), or more commonly, bits
393 per AP:

$$\widehat{I_{AP}^E} = \frac{1}{\bar{\lambda}}\sum_{i=1}^{N} \lambda_i p_X(x_i) \log_2 \frac{\lambda_i}{\bar{\lambda}} \qquad\qquad 5$$

394 Therefore, these two key metrics of spatial information are defined completely by quantities that can be
395 experimentally measured: the mean firing rate $(\bar{\lambda})$ from the AP counts over the duration of the
396 recording, the AP firing rate in the ith bin from the average rate map (λ_i), and the probability that the
397 animal is in the ith spatial bin from the normalized occupancy map $(p_X(x_i))$. The quantity of and noise
398 in these measurements affects the quality of the metric: in particular, undersampling due to low firing
399 rates or low trial counts induces a substantial positive bias (Treves and Panzeri, 1995).

400 In the derivation of these metrics, there are two key assumptions that are violated by functional
401 fluorescence recordings. First, the recordings do not follow Poisson statistics: instead of discrete counts
402 of APs (y), the functional fluorescence traces consists of a continuous relative change in fluorescence
403 $(\Delta F/F)$, and instead of a firing rate map (λ_i) measured in Hz, average intensity maps in units of $\Delta F/F$
404 are generated. The stationarity assumption is also violated: due to the slow decay, a time sample of the
405 fluorescence traces depend on the previous samples. The violation of these assumptions by functional
406 fluorescence recording will affect the precision and induce biases in the SMGM information metrics.
407 Since these effects have not previously been addressed or quantified, we measured these biases here
408 using a simulation study.

409 *Building a ground truth library of 10,000 neurons with known values of information*

410 To create a neuron with a known, ground truth information value, it was necessary to generate a
411 continuous (i.e. infinitesimally small bins) rate map $(\lambda(x))$ matching the desired information. To do this,
412 we first normalized the track length to 1 and assumed the animal's occupancy map to be spatially
413 uniform $\left(p_X(x_i) = \frac{1}{N}\right)$. We then created an exponentiated cubic spline with 5 randomly positioned nodes
414 (Figure 1A) to build a starting continuous map of the normalized instantaneous firing rate, $\frac{\lambda}{\bar{\lambda}}(x)$, with
415 the integral normalized to 1. We calculated the ground truth amount of information in bits per AP as
416 follows:

13

$$I_{AP}^E = \int_0^1 \frac{\lambda}{\bar{\lambda}}(x) \log_2\left(\frac{\lambda}{\bar{\lambda}}(x)\right) dx \qquad\qquad 6$$

417   The locations of the 5 nodes were then systematically varied [see Methods] to minimize the squared
418   error between the value calculated in Equation 6 and a target amount of information (Figure 1A,B), in
419   the end resulting in a mean error of 5.1*10^-9 bits/AP and a mean absolute error of 1.5*10^-7 bits/AP.
420   The rate map at this convergence point was used for further analysis. This procedure was repeated to
421   generate 10,000 mock neurons with a range of (known and ground truth) information values. Note that
422   the value in Equation 5 cannot be higher than when all the APs arrive in one spatial bin; the rate in that
423   bin is $N\bar{\lambda}$. If we assume uniform occupancy $\left(p_X(x_i) = \frac{1}{N}\right)$, then the maximum measureable information
424   is $\log_2 N$, in our case, 5.9 bits/AP with N=60 bins. Thus, the information values considered here range
425   between 0 and 6 bits/AP (Figure 1C). We chose a mean firing rate $(\bar{\lambda})$ for the neurons between 0.1 and
426   30 Hz, a range observed for a variety of different cortical and hippocampal neurons during behavior
427   (Buzsáki and Mizuseki, 2014; DeWeese et al., 2008; O'Connor et al., 2010; Roxin et al., 2011; Shafi et
428   al., 2007). From Equations 4-5, the ground truth information in bits per second is $I_s^E = \bar{\lambda} I_{AP}^E$. I_s^E for these
429   choices resulted in ground truth information values between I_s^E =0 and I_s^E =24 bits/sec (Figure 1C).
430   Example low (I_{AP}^E=0.04 bits/AP) and mid (I_{AP}^E=2 bits/AP) rate maps are shown in Figure 1D.

431   These rate maps provided a basis for generating mock AP firing data (and functional fluorescence data,
432   see below). Under real experimental conditions, recording duration and bin sizes are finite and animal
433   occupancy maps $(p_X(x_i))$ are not spatially uniform. These experimental limitations add error to the
434   estimate of a neuron's ground truth information value. Therefore, in order to accurately re-create these
435   limitations in our simulation study, we used real behavior datasets from head-restrained mice running
436   along a 3 m virtual linear track for water rewards (acquired as in Sheffield et al., 2017; Sheffield and
437   Dombeck, 2015). Unless otherwise indicated, all values reported will be the mean±standard deviation.
438   We selected at random from a library of 574 behavior sessions from mice navigating along familiar
439   tracks and concatenated and truncated these sessions to create behavior sessions uniformly sampled up
440   to 60 minutes in duration (average 30.2±17.1 minutes), resulting in an average 132 ± 71.2 laps per
441   session and an average running speed of 19.3 + 3.87 cm/sec (Figure 1E.1). This behavior, the average
442   firing rate $(\bar{\lambda})$, and the normalized rate map $(\frac{\lambda}{\bar{\lambda}}(x))$ from the mock neurons were used to create an
443   instantaneous firing rate trace (Figure 1E.2), sampled at 1 kHz, from which AP times were generated
444   assuming Poisson firing statistics (Figure 1E.3). An example mock of spiking in response to behavior
445   for low (0.04 bits/AP) and mid (2 bits/AP) information neurons can be seen in Figure 1F-H. From these
446   spiking responses, we then generated mock fluorescence traces by convolving the raster with a double-
447   exponential kernel matching the rise and fall times for GCaMP6f (Chen et al., 2013, Figure 1E.4) and
448   adding random Gaussian noise to model shot noise. Mock fluorescence traces for the two example
449   neurons in Figure 1F-H can be seen in Figure 1I-J. The mock AP and fluorescence traces were used to

14

450   create session mean spatial maps – of binned firing rate (λ_i in Hz) and change in fluorescence (f_i in $\Delta F/$
451   F), for information analyses (Figure 1K). By repeating this process, we built a large dataset of spiking
452   and fluorescence traces, generated from our library of mock neurons with known amounts of
453   information and using real animal spatial behavior. With tens of thousands of these mock neuron
454   recordings, we could then assess the effects of many simulation parameters on the information values
455   determined from the metrics including firing rate, session duration, fluorescence kernel shape, and
456   ground truth information value.

457   *Quantification of the accuracy and precision of the SMGM bits per second metric using functional*
458   *fluorescence recordings*
459   We first applied the SMGM bits per second metric ($\widehat{I_s^E}$) to our mock AP recording traces to verify that
460   they can recover our ground-truth information values given finite recording durations and bin sizes, and
461   non-uniform animal occupancy maps ($p_X(x_i)$). Figure 2A shows three mock neurons with ground truth
462   information values of $I_s^E =3$, 15 and 23 bits/sec. When the SMGM bits per second metric ($\widehat{I_s^E}$) was
463   applied to the AP traces from these example neurons, the information was well recovered, with $\widehat{I_s^E}=2.8$,
464   15 and 24 bits/sec, respectively. The results from these examples also held across the full 10,000 mock
465   neuron library (Figures 2B-D), as a linear fit (y-intercept = 0.093 ± 0.040, intercept p=$4.6*10^{-6}$ bits per
466   second and slope = 0.97 ± 0.0030, slope p$<<0.01$) explained nearly all the variance ($R^2 = 0.97$), the
467   average error was 0.22 ± 1.25 bits per second ($1.0\pm0.69\%$ error) and the absolute error was 0.64 ± 1.05
468   bits per second ($8.4\pm0.69\%$ error). There is a substantial positive bias for the lowest firing rates and
469   smallest number of trials (Figure 2-1A-B) which has been previously well characterized (Treves and
470   Panzeri, 1995), with average errors exceeding +10% for less than 6 minutes of recording, mean rate
471   under 0.6 Hz, and under 11 trials. Thus, the SMGM bits-per-second metric ($\widehat{I_s^E}$) recovers the ground-
472   truth information well using AP recordings, with the only error coming from finite recording time and
473   variable animal behavior.

474   We next discuss the changes to the SMGM bits per second metric ($\widehat{I_s^E}$) commonly used for application
475   to functional fluorescence traces (Hainmueller and Bartos, 2018; Heys and Dombeck, 2018), and
476   explore the implications of these changes. Most simply, the mean firing rate ($\bar\lambda$) and the mean firing rate
477   in a spatial bin (λ_i) are replaced by the mean change in fluorescence ($\bar f$) and the mean change in
478   fluorescence in a bin (f_i). Making these substitutions in Equation 4 results in the information as
479   measured by functional fluorescence:

$$\widehat{I_s^F} = \sum_{i=1}^{N} f_i p_X(x_i) \log_2 \frac{f_i}{\bar f} \qquad\qquad 7$$

480   The fluorescence map f_i differs from the firing rate map λ_i in two ways. First, the fluorescence map is
481   approximated by the firing rate map scaled by a factor c, dependent on the height and width of the

15

482   kernel and measured in units of $\frac{\Delta F/_F}{Hz}$, and second it is smoothed by the kernel (Figure 1E4). If we

483   discount the latter for a moment and focus on the scaling, $f \approx c\lambda$, we can see that substituting λ with $c\lambda$

484   in Equation 4 results in $\widehat{I_s^F} = c\widehat{I_s^E}$. The units for $\widehat{I_s^F}$ are no longer in bits per second, as it has previously

485   been reported (Hainmueller and Bartos, 2018), but are instead in units of $\frac{bits\,^{\Delta F}/_F}{sec\,Hz}$ or $\frac{bits\,^{\Delta F}/_F}{AP}$, which are

486   difficult to interpret (see *Guidelines for application of information theoretic metrics to functional*

487   *fluorescence imaging data* section for further discussion). The effect of smoothing is difficult to

488   analytically quantify since it both alters c by changing the average intensity and distorts the firing rate

489   map. Therefore, to fully quantify the impact of convolving an AP recording with a functional

490   fluorescence kernel on recovering ground truth information, we used our mock fluorescence traces.

491   We applied a GCaMP6f modeled kernel to the 10,000 mock AP traces to generate 10,000 mock

492   fluorescence calcium traces. Figure 2A shows the fluorescence traces generated from three mock

493   neurons with ground truth information values of I_s^E =3, 15 and 23 bits/sec. The effects of the

494   convolution can be seen in the differences in scaling and shape between the fluorescence maps f_i and the

495   firing rate maps λ_i. When the fluorescence metric ($\widehat{I_s^F}$) was applied to the fluorescence traces from these

496   example neurons, the information recovered was $\widehat{I_s^F}$ = 0.13, 0.47 and 1.1 $\frac{bits\,^{\Delta F}/_F}{AP}$, respectively,

497   indicating significant deviation from the ground truth information values assuming the units are

498   comparable. The results from these examples also held across the full 10,000 mock neuron library

499   (Figures 2E-G), as there was a clear scaling of the ground truth information and a consistent

500   underestimation with a mean error of -11.1$\pm$6.7 AU (-96.0$\pm$1.3% error). The best-fit line of the

501   measured information ($\widehat{I_s^F}$) versus the ground truth information (I_s^E) had an intercept near 0

502   (0.0029$\pm$0.0016 $\frac{bits\,^{\Delta F}/_F}{AP}$, p=0.07). The slope of this fit was 0.039$\pm$12e-4 $\frac{\Delta F/_F}{Hz}$ (p<<0.01), which

503   provides a measure of the scaling factor (c). This error was not corrected for with denser sampling: it

504   remained consistent even at high firing rates and many trials (Figure 2-1C-D). In addition to this scaling

505   effect caused by c, smoothing of the rate map could induce nonlinearity in the relationship between $\widehat{I_s^F}$

506   and I_s^E. To test for such an effect, we fit the measured information in Figure 2E with a saturating

507   exponential and compared the fits using a likelihood ratio test: the exponential did not significantly

508   improve the fit (χ_1^2=0.093, p=0.76), which indicates that smoothing by the kernel does not induce

509   significant nonlinearities. c is dependent on the height and width (the integral) of the kernel and was

510   measured here as 0.039$\pm$12e-4 $\frac{\Delta F/_F}{Hz}$. The consistent, negative bias observed in estimating information

511   with $\widehat{I_s^F}$ (Figure 2E) would be easy to correct for assuming the c factor, and therefore the kernel, were

512   similar across all measured neurons. This point is considered further in the *Guidelines for application of*

513   *information metrics to functional fluorescence imaging data* section below. We conclude that ground

514   truth information, as measured by the fluorescence SMGM bits per second metric ($\widehat{I_s^F}$), is transformed

515   into different units and is linearly scaled by a factor c dependent on the height and width of the kernel.

16

516 The amplitude (height) of the change in fluorescence can vary across indicators and conditions. The
517 height of the kernel, given a constant kernel width, should linearly scale c and the error in estimating
518 information with $\widehat{I_s^F}$. To explicitly test this prediction, we simulated an additional 5,000 fluorescence
519 traces with kernels of varying height (0-3 $\Delta F/F$, Figure 2I-K), but that maintain the same shape and
520 width (from the GCaMP6f kernel), and then measured the percent error in estimating information with
521 $\widehat{I_s^F}$. As observed above for the GCaMP6f example (Figure 2 E-G), the percent error in estimating
522 information with $\widehat{I_s^F}$ shows little dependence on ground truth information (Figure 2I-K). However, as a
523 function of the height of the kernel, the percent error (averaged over all ground truth information values)
524 in estimating information with $\widehat{I_s^F}$ is fit well with an increasing linear function (intercept = -99.8$\pm$0.42%,
525 intercept p<<0.01, slope 20.7 $\pm$0.14%/$\frac{\Delta F}{F}$, slope p<<0.01, R^2= 0.80; Figure 2I-J). Over the wide array of
526 available functional fluorescent indicators in use today (Figure 2H), this leads to differences in error due
527 to differences in transient height of the indicator used alone. For the indicators shown in Figure 2H,
528 there is an average height of 0.603$\pm$0.10 SD $\Delta F/F$: the error spans from -95.8% for the kernel height
529 reported for gCamp6f (0.19 $\Delta F/F$) to -88.2% for gCamp7f (0.56 $\Delta F/F$). It should be noted that
530 fluorescence ($\Delta F/F$) is always reported here as a fractional change, not as a percentage (% $\Delta F/F$); if a
531 kernel height of 19 % $\Delta F/F$ is used, the units would again change. Thus, as expected, the percent error
532 in estimating information with the SMGM bits per second estimator ($\widehat{I_s^F}$) scales linearly with the height
533 of the kernel.

534 The width of the kernel can vary widely across fluorescent indicators (Figure 2H), with "faster"
535 indicators boasting shorter rise and fall times. The combined effect of a longer rise and fall time is to
536 smooth and delay the AP train; in other words, it acts as a causal low-pass filter. The cutoff period of
537 this low pass filter provides a measurement of the effective width of the kernel [see Methods]. The effect
538 of such differences in kernel shape on the error in estimating information with $\widehat{I_s^F}$ is difficult to measure
539 analytically. We therefore simulated an additional 5,000 fluorescence traces with kernels of different
540 kernel widths (but constant height of the GCaMP6f kernel), resulting in a range of kernel durations (rise
541 times: 1 ms to 1 second, fall times longer than the rise time up to 2 seconds), and then we measured the
542 percent error in estimating information with $\widehat{I_s^F}$. Similarly, as observed above for the GCaMP6f and
543 varying kernel height examples (Figure 2 E-K), the percent error in estimating information with $\widehat{I_s^F}$
544 shows little dependence on ground truth information (Figure 2N). Interestingly, the percent error
545 (averaged over all ground truth information values) in estimating information with $\widehat{I_s^F}$ shows a complex
546 nonlinear response as a function of the width of the kernel (Figure 2L-M). The error increases up to a
547 kernel width of ~3 seconds, at which point it saturates at ~ -85% error. This arises from an interaction
548 between changing the average value of the original AP trace and flattening the average fluorescence
549 map (f_i). Over the wide array of available functional fluorescent indicators in use today, this leads to
550 differences in error due to differences in width of the indicator used alone. For example, an average
551 error of -97.1$\pm$0.63% were observed for iGluSnfR, the shortest indicator considered here at 0.52
552 seconds. For gCamp6s, the slowest indicator examined (2.54 seconds), the average was -89.6$\pm$4.6%. To

17

553 estimate the percent errors for these five indicators considering differences in *both* height and duration,
554 we used these 5 kernels to generate mock fluorescence traces from the 10,000 neurons in Figure 2B-G.
555 The resulting distributions, estimated c values, and mean and absolute errors can be seen in Figure 2-2.
556 In summary, we conclude that information, as measured by the fluorescence SMGM bits per second
557 metric ($\widehat{I_s^F}$), is transformed into different units and is linearly scaled by a factor (c) dependent on the
558 height and width of the kernel, with c linearly dependent on height and nonlinearly dependent on width.
559 The error induced by these transformations changes substantially over the range of kernel values of the
560 different functional indicators widely used today, and therefore these are important factors to consider
561 when designing and interpreting functional imaging experiments (see *Guidelines for application of*
562 *information metrics to functional fluorescence imaging data* for further discussion).

563 *Quantification of the accuracy and precision of the SMGM bits per AP metric using functional*
564 *fluorescence recordings*
565 The SMGM metric is commonly normalized by the mean rate to obtain a measurement in units of bits
566 per AP. We thus applied the SMGM bits per AP metric ($\widehat{I_{AP}^E}$) to our mock AP recording traces to verify
567 that they can recover our ground-truth information values. Figure 3A shows three mock neurons with
568 ground truth information values I_{AP}^E =0.05, 1.8 and 4.2 bits/AP. When the SMGM bits per AP metric
569 ($\widehat{I_{AP}^E}$) was applied to the AP traces from these example neurons, the information was well recovered,
570 with $\widehat{I_{AP}^E}$=0.06, 1.8 and 4.2 bits/AP respectively. The results from these examples also held across the
571 full 10,000 mock neuron library (Figures 3B-D), as a linear fit (y-intercept = 0.087$\pm$0.029, intercept
572 p=2.8e-184 bits per second and slope = 0.93 $\pm$0.0010, slope p<<0.01) explained nearly all the variance
573 ($R^{2 =}$ 0.99), the average error was -0.071$\pm$0.23 bits per AP (3.2$\pm$5.9% error) and the absolute error was
574 0.13$\pm$0.21 bits per second (8.1$\pm$9% error). However, the data was better fit with a saturating
575 exponential (χ_1^2=1.6e3, p<<0.01) converging to 5.8 bits/AP as it approached the limit due to the finite
576 bin count. There is a substantial positive bias for the lowest firing rates and smallest number of trials
577 (Figure 2-1E-F) which has been previously well characterized (Treves and Panzeri, 1995). Thus, the
578 SMGM bits per-AP metric ($\widehat{I_{AP}^E}$) recovers the ground-truth information well using AP recordings
579 (except at the largest ground truth information values), with the primary error coming from finite
580 recording time and variable animal behavior.

581 We next discuss the changes needed to apply the SMGM bits per AP metric ($\widehat{I_{AP}^E}$) to functional
582 fluorescence traces and explore the implications of these changes. Most simply, the mean firing rate ($\bar{\lambda}$)
583 and the mean firing rate in a spatial bin (λ_i) are replaced by the mean change in fluorescence ($\bar{f}$) and the
584 mean change in fluorescence in a bin (f_i). Making these substitutions in Equation 5 results in the
585 information as measured by functional fluorescence:

18

$$\widehat{I_{AP}^F} = \frac{1}{\bar{f}} \sum_{i=1}^{N} f_i p_X(x_i) \log_2 \frac{f_i}{\bar{f}} \qquad\qquad 8$$

586 As discussed above, the fluorescence map (f_i) can be approximated as a scaled version of the rate, that
587 is, $f = c\lambda$ and $\bar{f} = c\bar{\lambda}$. Thus, under this approximation, the c factors in Equation 8 cancel, leading to $\widehat{I_{AP}^F}$
588 equivalent to $\widehat{I_{AP}^E}$, with the same units of bits/AP. This, of course, ignores the fact that the kernel smooths
589 the rate map, leading to a bias in the metric that is difficult to quantify analytically.

590 We then applied the fluorescence SMGM bits per AP metric ($\widehat{I_{AP}^F}$) to our 10,000 mock GCaMP6f traces.
591 Figure 3A shows the fluorescence traces generated from three mock neurons with ground truth
592 information of I_{AP}^E=0.05, 1.8 and 4.2 bits/AP. When the fluorescence metric ($\widehat{I_{AP}^F}$) was applied to the
593 fluorescence traces in these examples, the information recovered was 0.04, 1.8 and 3.5 bits/AP,
594 indicating some deviations – especially for the highest information neuron. These results held for the
595 10,000 mock neuron library (Figure3E-G). At low information values, there was little bias, but at higher
596 information values the information recovered was substantially lower than the ground truth information.
597 The mean resulting error was -0.38$\pm$0.58 bits/AP (-9.7$\pm$27.8%) and absolute error of 0.39
598 (12.9$\pm$26.4%). This error was better fit with a saturating exponential than a linear fit (χ_1^2=1.6e3,
599 p<<0.01), with the average error less than 5% up to ground truth information of 1.8 bits/AP and less
600 than 10% up to 3.0 bits/AP. At ground truth information values higher than 3 bits/AP, the average error
601 was -1.06$\pm$0.595 (-22.5$\pm$9.44%) and absolute error was 1.07$\pm$0.589 bits/AP (22.6$\pm$9.21%). This error
602 persisted even with denser sampling: it remained consistent even at high firing rates and many trials
603 (Figure 2-1E-F). Thus, the indicator induces relatively little error at lower information values (<3
604 bits/AP), but the smoothing effect of the kernel induces a nonlinear, negative bias to the estimator,
605 particularly at ground truth information values over 3 bits/AP.

606 Although the height of the kernel can vary between different functional fluorescence indicators (Figure
607 2H), these height variations linearly scale the fluorescence map. Thus, since $\widehat{I_{AP}^F}$ involves normalization
608 by the mean change in fluorescence ($\bar{f}$), $\widehat{I_{AP}^F}$ should not depend on kernel height. To explicitly test this
609 prediction, we used the 5,000 fluorescence traces described in the previous section (Quantification of the
610 accuracy and precision of the SMGM bits per second metric using functional fluorescence recordings),
611 with kernels of varying height (0-3 ΔF/F), but that maintain the same shape and width (from the
612 GCaMP6f kernel). Then, we measured the percent error in estimating information with $\widehat{I_{AP}^F}$ (Figure 3H-
613 J). Unlike for the SMGM bits per second metric, the percent error (averaged over all ground truth
614 information values) in estimating information with $\widehat{I_{AP}^F}$ shows little or no dependence on the height of the
615 kernel (p=0.43), but a nonlinear dependence on ground truth information as in Figure 3E-G, with no
616 significant difference in the parameters of the saturating exponential fit (χ_2^2=1.67, p=0.43). Thus, as

19

617   expected, the percent error in estimating information with the SMGM bits per AP metric ($\widehat{I_{AP}^F}$) does not
618   vary with the height of the kernel.

619   With little effect of kernel height on $\widehat{I_{AP}^F}$, the width of the kernel likely drives biases in the metric. We
620   thus used the 5,000 fluorescence traces generated from a range of different kernel durations (rise times:
621   1 ms to 1 second, fall times longer than the rise time up to 2 seconds; but constant height of the
622   GCaMP6f kernel) from the previous section (*Quantification of the accuracy and precision of the SMGM*
623   *bits per second metric using functional fluorescence recordings*), and then we measured the percent
624   error in estimating information with $\widehat{I_{AP}^F}$ (Figure 3 K-M). Similarly, as observed above for GCaMP6f and
625   the varying kernel height examples (Figure 3E-J), the percent error in estimating information with $\widehat{I_S^F}$
626   shows a nonlinear dependence on ground truth information (Figure 3E-G). The percent error (averaged
627   over all ground truth information values) showed a nonlinear response as a function of the width of the
628   kernel (Figure 3K-L), with a steep increase in error for kernel widths >~1 second. Even for kernel
629   widths <~1 second, the percent error was strongly dependent on the ground truth information value, with
630   steep increases in error for values >~2.5-3 bits/AP (Figure 3M). Thus, as the kernels gets wider, there is
631   more negative bias at lower and lower information measured. The resulting errors are thus larger for
632   wider kernel indicators: for example, with a kernel width the same as gCaMP6s (2.54s), the error
633   exceeds -17% even at low (<0.25 bits/AP) information, with average errors of -0.86$\pm$1.0 bits/AP (-
634   31$\pm$19% error) and absolute errors of 0.87$\pm$1.0 bits/AP (32.6$\pm$16% error). In contrast, with a kernel
635   width the same as iGluSnfR (0.52 seconds), the average error exceeded 5% at 3 bits per AP and 10% at
636   3.7 bits per AP with a mean error of -0.57$\pm$1.00 (-8.0$\pm$14%) bits/AP and absolute error of 0.41$\pm$ 0.56
637   bits/AP (11$\pm$11%). To estimate the percent errors for the five indicators shown in Figure 2H, taking into
638   account differences in *both* height and duration, we used the 5 kernels to generate mock fluorescence
639   traces from the 10k neurons in Figure3B-G. The resulting distributions, mean and absolute errors, and
640   error thresholds can be seen in Figure 3-1.

641   Since the known information values in our library of 10,000 mock neurons were determined using the
642   SMGM metric, which includes the assumption that neuron firing follows an inhomogeneous Poisson
643   process, we next investigated whether the biases observed between AP and fluorescence metrics ($\widehat{I_S^E}$
644   versus $\widehat{I_S^F}$ and $\widehat{I_{AP}^E}$ versus $\widehat{I_{AP}^F}$; Figures 2 and 3) in our mock neuron datasets were also observed in real
645   neuron recordings (i.e. real spiking that could deviate from Poisson firing).We therefore measured
646   information in a real spiking dataset from hippocampal neurons in rats running on a behavioral track
647   (Chen et al., 2016; Grosmark and Buzsaki, 2016; Grossmark et al., 2016). We generated mock
648   fluorescence traces as we did with simulated AP trains from our mock neurons, compared the
649   information measured from APs versus fluorescence ($\widehat{I_S^E}$ versus $\widehat{I_S^F}$ and $\widehat{I_{AP}^E}$ versus $\widehat{I_{AP}^F}$) in the real neuron
650   recordings and found that the biases were largely consistent with the simulated mock neuron datasets
651   (Figure 5-1).

20

652   In summary, we conclude that ground truth information, as measured by the fluorescence SMGM bits
653   per AP metric ($\widehat{I_{AP}^F}$), retains the units and insensitivity to height scaling of the electrophysiological
654   metric ($\widehat{I_{AP}^E}$), but is nonlinearly biased by the smoothing of the fluorescence map dictated by the width of
655   the kernel. The estimation errors strongly depended on both the width of the kernel and the information
656   value being measured. Since these parameters change substantially over the different functional
657   indicators and different neuron types and behaviors that are commonly used today, they are important
658   factors to consider when designing and interpreting functional imaging experiments (see below for
659   further discussion).

660   *Nonlinearity introduces further biases*
661   The results presented in the previous two sections rely on the approximation that $\Delta F/F$ scales linearly
662   with the firing rate, which is not strictly true in practice (Dana et al., 2018; Éltes et al., 2019; Greenberg
663   et al., 2018). Calcium imaging can be more responsive to bursts of APs rather than isolated spikes, and
664   saturates at high firing rates. As an example for how to examine how nonlinearities between $\Delta F/F$ and
665   firing rate could affect the fluorescence SMGM metrics ($\widehat{I_S^F}$ and $\widehat{I_{AP}^F}$), we applied a log-sigmoid
666   nonlinearity (Figure 3-3A) to the 10,000 mock GCaMP6f time-series traces described above, based on
667   the real behavior of GCaMP6f in cultured neurons (Dana et al., 2019, see Methods). While the resulting
668   measurements (Figure 3-3) of ground truth information, as measured by the fluorescence SMGM
669   metrics, are largely consistent with the results observed when using the linear assumption (Figures 2 and
670   3), some quantitative difference can be seen. Thus, even a relatively simple nonlinearity between $\Delta F/F$
671   and firing rate can add distortions to the amount of information measured using the fluorescence SMGM
672   approach.

673   *Deconvolution may not be sufficient to eliminate biases*
674   The framework presented here for comparing ground truth information with information measured with
675   the SMGM metrics can be extended to test the efficacy of other strategies for extracting mutual
676   information. In particular, a perfect AP inference method would alleviate the problems associated with
677   applying the SMGM metrics to functional fluorescence recordings. To test the utility of such a strategy
678   in measuring information, we applied a popular deconvolution algorithm, FOOPSI (Vogelstein et al.,
679   2010, see Methods), to the same 10,000 mock GCaMP6f time-series traces described above.
680   Importantly, this deconvolution algorithm (and other available algorithms) does not recover traces of
681   relative spike probability or exact spikes times, but instead produces sparse traces with arbitrary units,
682   that have non-zero values estimating the relative 'intensity' of spike production over time (d). This
683   signal can be thought of as a scaled estimate of the number of spikes per time bin, and thus the average
684   intensity map will have some similar properties to the florescence intensity maps – that is, we would
685   expect the intensity maps from deconvolution to approximate the relative firing rate scaled by some
686   factor c, which has arbitrary units.

21

687 We then measured information in these deconvolved d-traces using the SMGM metrics ($\widehat{I_S^d}$ and $\widehat{I_{AP}^d}$),

688 which are identical to ($\widehat{I_S^F}$ and $\widehat{I_{AP}^F}$), except SMGM is applied to d-traces instead of functional

689 fluorescence traces. When using the SMGM bits per second measure ($\widehat{I_S^d}$, Figure 4A), we found a clear

690 scaling of the ground truth information. The scaling factor was very small (c=1.15e-3±1.8e-5 A.U.),

691 resulting in low predicted information (mean error -11.4±6.92 AU, mean % error -99.8±0.38%). This

692 error was larger than when we measured information directly from the florescence traces using $\widehat{I_S^F}$

693 (Figure 2E; 96.0% absolute error, Ranksum p<<0.01; c=0.0390). It is worth noting that the deconvolved

694 trace d can be arbitrarily scaled, so in a sense this error is arbitrary. However, these are the results from

695 the scaling chosen by a widely used deconvolution algorithm and the large error emphasize that the scale

696 of d can have a large effect on the bits per second measure ($\widehat{I_S^d}$).

697 Assuming that the intensity map of the deconvolved d-traces are a scaled version of the true rate maps,

698 we could measure information using the SMGM bits per AP metric $\widehat{I_{AP}^d}$ without changing units (Figure

699 4B). Compared to the SMGM bits per AP metric applied to florescence (I_{AP}^F), on average there was

700 some reduction in the nonlinearity at higher ground truth information (I_{AP}^E) values when using $\widehat{I_{AP}^d}$,

701 resulting in linear fits closer to the unitary line ($\widehat{I_{AP}^d}$ slope $= 1.02 \pm 0.0027$, $R^2 = 0.76$ versus $\widehat{I_{AP}^F}$ slope

702 $= 0.78\pm0.0011$, R^2=0.93). However, information measured with $\widehat{I_{AP}^d}$ was still better fit with a saturating

703 exponential (χ_1^2=2.3e3, p~0) converging to a saturation value of 5.51 bits per AP (compared to 5.78 for

704 $\widehat{I_{AP}^F}$), as expected since the algorithm is not expected to resolve spikes at orders of magnitude shorter

705 timescales than the kernel. This resulted in a positive bias at lower levels of ground truth information.

706 For ground truth information values below 3 bits per AP, the average error for $\widehat{I_{AP}^d}$ was 0.556±0.50 bits

707 per AP (68.9±104%) compared to -0.060±0.13 bits per AP (2.75±0.36%) for $\widehat{I_{AP}^F}$. For ground truth

708 information values above 3 bits per AP, the average error for $\widehat{I_{AP}^d}$ was -0.127±0.76 bits per AP (-

709 1.0±16.8%) as compared to -1.04±0.59 bits per AP (-0.22±9.4%) for $\widehat{I_{AP}^F}$. Overall, there was more error

710 when the SMGM bits per AP metric was applied to deconvolved data compared to when applied directly

711 to fluorescence traces ($\widehat{I_{AP}^d}$ mean absolute error 0.60±0.47 bits/AP (52.7±89.1%) vs $\widehat{I_{AP}^F}$ was 0.13±0.21

712 bits per second (8.1±9% error), Ranksum p<<0.01). Thus, when comparing the recovery of ground truth

713 information from functional fluorescence traces using either direct application of the SMGM metrics ($\widehat{I_S^F}$

714 and $\widehat{I_{AP}^F}$) or the application of the SMGM metrics to deconvolved z-traces ($\widehat{I_S^d}$ and $\widehat{I_{AP}^d}$), we found better

715 recovery using the direct application approach ($\widehat{I_S^F}$ and $\widehat{I_{AP}^F}$).

716 *The KSG and Binned Estimators are poor estimators of MI in functional florescence data*

717 In addition to SMGM, the KSG and Binned Estimation metrics have been developed for estimating

718 mutual information between variables. These other two metrics produce information measured in bits

719 per second, so they are only comparable to the SMGM bits per second estimator ($\widehat{I_S^F}$). The KSG metric

22

720 uses the kth nearest neighbor distances between points in the neural response and behavioral variable
721 space to estimate information (Kraskov et al., 2004). The Binned Estimation metric uses discrete bins to
722 estimate the full multidimensional joint probability distribution ($p_{(X,Y)}$ in Equation 1) to estimate mutual
723 information (Timme and Lapish, 2018). These two metrics estimate information across time samples
724 and therefore are dependent on firing rate like the SMGM bits/sec metric considered above. Further, the
725 Binned Estimator is sensitive to the precise method used for data binning, and thus we have used two
726 commonly applied binning methods: uniform and occupancy based bins.

727 We applied the KSG, Binned Estimator (Uniform bins), and Binned Estimator (Occupancy binned) (see
728 *Methods*) to the same 10,000 mock GCaMP6f time-series traces and behavioral data used to assess the
729 SMGM approach. These methods all behaved similarly when applied to our simulations (Figure 4C-E),
730 so they will be discussed together here. The information values measured by these techniques correlated
731 with ground truth information in bits per second (I_S^E). Interestingly, unlike the SMGM bits per second
732 metric ($\widehat{I_S^F}$, Figure 2), the KSG and Binned Estimator results were better fit with a saturating exponential
733 than with a linear fit (χ_1^2=1.70e4, 3.12e4, and 3.14e4 respectively, p~0). The KSG and Binned Estimator
734 methods overestimated the information at lower ground truth (I_S^E) values and saturated quickly at higher
735 values. For ground truth information (I_S^E) values below 10 bits per second, the mean absolute errors were
736 10.3±7.82 bits per second (465±4,390%), 22.2±12.6 bits per second (821.7±3,353%), and 24.2±14.0
737 bits per second (911±3,926%) for the KSG, Binned Estimator (Uniform bins), and Binned Estimator
738 (Occupancy binned) respectively (Figure 4F). This is in comparison to the 0.35±0.59 $\frac{bits\ \Delta F/_F}{AP}$
739 (14±103%) mean absolute error found using the SMGM bits per second metric ($\widehat{I_S^F}$) for ground truth
740 information values less than 10 bits per second. For ground truth information (I_S^E) values greater than 10
741 bits per second, the mean absolute errors were 13.2±8.66 bits per second (85.0±64.4%), 25.4±16.2 bits
742 per second (165.2±118.3%) and 28.9±17.34 bits per second (186.3±124.9%) for the KSG, Binned
743 Estimator (Uniform bins), and Binned Estimator (Occupancy binned) respectively. This is in comparison
744 to the 0.97±1.15 bits per second (5.85±6.73%) mean absolute errors found using the SMGM bits per
745 second metric ($\widehat{I_S^F}$) for ground truth information values greater than 10 bits per second. Over the full
746 range of ground truth values, mean absolute errors of 11.9±8.42 bits per second (254.8%), 23.5±14.8
747 bits per second (456.7%) and 26.7±16.1 bits per second (509.0%) were found for the KSG, Binned
748 Estimator (Uniform bins), and Binned Estimator (Occupancy binned) respectively – an order magnitude
749 larger than the 2.4±2.97 AU (22±27% error) error seen using the SMGM bits per second metric ($\widehat{I_S^F}$).
750 As a control, we applied the Binned Estimators to AP traces and compared the estimated information to
751 the ground truth information to verify that the large errors observed (Figure 4 D,E) were caused when
752 the estimators were applied to fluorescence data (rather than simply a difference between the Binned
753 Estimator, which do not rely on a Poisson firing assumption, and the ground truth information
754 established using SMGM, which does rely on a Poisson firing assumption). We found the errors when
755 applying the Binned Estimators to AP traces were relatively small (Figure 4-2, mean absolute error
756 2.72±3.38 bits per second (41.1%) and 2.70±3.33 bits per second (41.0%) for the uniform and

23

757 occupancy based binning respectively). Therefore, when comparing the recovery of ground truth
758 information from functional fluorescence traces using either the SMGM metric $\widehat{I_S^F}$ or the KSG and
759 Binned Estimator metrics, we found better recovery using the SMGM approach ($\widehat{I_S^F}$).

760 *An analytic approximation can reproduce some qualitative, but not quantitative, results of the numeric*
761 *solutions*

762 Some of the general features of the relationship between ground truth information and fluorescence
763 SMGM metrics can also be seen using an analytic approximation. For example, if we approximate the
764 rate map as a Gaussian firing field with mean rate $\bar{\lambda}$, simplify the kernel approximation to a single
765 exponential with falloff τ, assume constant, normalized movement speed v, and assume that the
766 convolution between the kernel and the mean rate map is nearly Gaussian, we can approximate the
767 relationship between the bits per second ground truth information I_S^E and measured fluorescence
768 information I_S^F as

769 $$I_S^F \approx -\frac{Av\tau\bar{\lambda}\log\left(4^{-\frac{I_S^E}{\bar{\lambda}}+2\pi ev^2\tau^2}\right)}{\log(4)} \qquad 9$$

770 and between the bits per AP ground truth information I_{AP}^E and measured fluorescence information I_{AP}^F as

771 $$I_{AP}^F \approx -\frac{\log\left(4^{-I_{AP}^E+2e\pi v^2\tau^2}\right)}{\log(4)} \qquad 10.$$

772 Similar to the numerical solution, the analytic approximation provided by these equations (9 and 10)
773 predict that the fluorescence bits per second metric is dominated by a prefactor ($A\tau v\bar{\lambda}$ in the analytical
774 case), and that the fluorescence bits per action potential metric saturates at larger information values.
775 Our numerical solutions provide more accurate measures for the magnitude of these effects, and for the
776 magnitude of information values themselves, given that they include the more accurate double
777 exponential kernel, signal noise, and the realistic nonstationary speed, position and fluorescence signals.
778 These quantitative differences can be seen in Figure 4-3 where we directly compared this analytic
779 approximation to our numerical approach by simulating 10,000 neurons with Gaussian rate maps ($\lambda(x)$)
780 with known (ground truth) information. We found a significant difference in the slope of the bits per
781 second estimator (c, 0.041 vs 0.0036 $\frac{\Delta F/F}{Hz}$ for the numeric versus analytical respectively), likely due to
782 the nonstationarities present in behavior and florescence signals. For the fluorescence bits per AP
783 measure, the analytic approximation predicts a large positive bias for ground truth values up to ~4
784 bits/AP. This is in contrast to the numeric solution, which has less than 10% error for ground truth
785 information values below 3.12 bits/AP.

24

786 *Guidelines for application of information metrics to functional fluorescence imaging data*

787 Taken together, the above results suggest that across the information metrics applied directly to
788 functional fluorescence traces, the SMGM metrics provide the most reliable and interpretable
789 information measurements. We thus suggest the following guidelines for use and interpretation of the
790 SMGM metrics as applied to fluorescence mutual information metrics ($\widehat{I_s^F}$ and $\widehat{I_{AP}^F}$) defined in Equations
791 7 and 8.

792 The SMGM bits per second metric ($\widehat{I_s^F}$) is likely attractive to imaging researchers because the units
793 suggest that precise knowledge of AP numbers and times are not required for its use. However, there are
794 several challenges when applying the SMGM bits per second metric to functional fluorescence imaging
795 data. First, the substitution of the change in fluorescence map (f) for the AP firing rate map (λ)
796 introduces a change in units, from bits per second to $\frac{\Delta F}{F} \frac{bits}{AP}$, which is difficult to interpret and relate back
797 to bits per second. Second, the transformation of AP firing rate to change in fluorescence can be
798 approximated by a c scaling factor ($f = c\lambda$), which is measured in $\frac{\Delta F/F}{Hz}$, a quantity that is unknown *a*
799 *priori*. If c is not consistent between the neurons of a population of interest, then the information values
800 will be scaled differently and cannot be directly compared (Figure 2). Since c is dependent on the width
801 and height of the indicator response to a single AP (the kernel), it can vary from neuron to neuron based
802 on difference in indicator expression level, intracellular calcium buffering, and many other factors
803 (Aponte et al., 2008; Greenberg et al., 2018; Helmchen and Tank, 2015; Park and Dunlap, 1998). More
804 research will be needed to measure these parameters (e.g. Chen et al., 2012, 2013a), and thus c, across
805 neurons. Some results suggest that there may be non-trivial amounts of variability within a populations
806 of neurons (Éltes et al., 2019; Greenberg et al., 2018). With the impact of c on the SMGM bits per
807 second metric, and the possible variability of c across a population of neurons, how can researchers
808 properly extract useful measurements of information using $\widehat{I_s^F}$?

809 Guideline 1: First, we note that *if* experimental measurements reveal small and acceptable variations in c
810 across the neurons of interest, then the information values derived from $\widehat{I_s^F}$ can be normalized by this
811 factor to recover information values in units of SMGM bits per second (independent of $\Delta F/F$) that can
812 be compared across neurons.

813 Under the assumption of a consistent kernel, approximations for c for common indicators can be found
814 in Figure 2-2.

815 Guideline 2: Further, given small variations in c across the neurons of interest, the ratio of $\widehat{I_s^F}$ between
816 neurons in the population provides a meaningful metric for comparisons. For example, such ratios could
817 be used to divide a population of neurons accurately into groups based on their information values (e.g.
818 three quantiles of information) or compare the information values between different functional subtypes
819 of neurons (e.g. between place and non-place cells).

25

820 Guideline 3: The metric can still be useful even if experimental measurements reveal large and
821 unacceptable variations in c across the neurons of interest, or if experimental measurements of c do not
822 exist. In such cases, since it is reasonable to assume that c is consistent in the same neuron over time,
823 comparisons across the same neuron can provide meaningful insights by using a ratio of $\widehat{I_s^F}$ measured
824 (from the same neuron) across different conditions. For example, quantifying the neuron by neuron ratio
825 of $\widehat{I_s^F}$ between different behavioral states or conditions of an animal or task, such as between goal-
826 directed vs non-goal-directed running down a linear track, would allow researchers to make conclusions
827 such as the following: "The population of neurons in region Z carries X+/-Y times more information
828 during goal-directed than non-goal-directed running."

829 Therefore, we conclude that with careful consideration of the (known or unknown) variability of the
830 fluorescence response kernel (c), $\widehat{I_s^F}$ can be used to extract useful measurements of information, either
831 direct measurements of information across a population of neurons (with known and similar c), ratios of
832 information between different neurons of a population (with known and similar c) or differences across
833 different conditions within the same neuron (with c unknown or different across neurons).

834 The SMGM fluorescence bits per AP metric ($\widehat{I_{AP}^F}$) results in the same units as the AP based metric $\widehat{I_{AP}^E}$,
835 and therefore may provide imaging researchers with information values that are relatively easy to
836 interpret. However, this similarity in units is somewhat misleading since the number and timing of APs
837 are not directly measured with functional fluorescence traces and the asymmetric and relatively slow
838 dynamics of fluorescence indicators leads to shifting and smoothing of the AP rate map (λ). This issue
839 can have the effect of inducing a significant negative bias in information measurements, especially at
840 high information values and with functional indicators with wider kernels (Figure 3). This is the most
841 important factor to consider when determining how researchers can properly extract useful
842 measurements of information using $\widehat{I_{AP}^F}$. The shifting and smoothing of the AP rate map by fluorescence
843 effectively leads to crosstalk between adjacent spatial bins. Therefore, it is critical to consider the size of
844 the spatial bins in relation to the spatial shift and smoothing induced by the indicator (effectively the
845 kernel plotted in space, rather than time, using the animal's average running velocity to transform from
846 time to space). It is reasonable then to counteract the spatial shift and smoothing effect by using larger
847 bin sizes, but this only works up to a point since larger bins limit the maximum amount of information
848 possible to measure and may negatively bias the information values near this upper limit, even for AP
849 based recordings (Figure 3B-D). Researchers could potentially optimize the recovery of ground truth
850 information by appropriately selecting bin size for a particular indicator (see Figure 3-2 A-B).

851 In practice, using gCaMP6f and the rodent spatial behavior and spatial bin sizes (5cm) used here, our
852 analysis suggests that $\widehat{I_{AP}^F}$ provides reasonable measurements of information for neurons with values up
853 to 3 bits per AP (Figure 3E-G) since this is the point where the absolute error exceeds 10% (comparable
854 to the mean absolute error when measuring information from AP data (8.4%)). Equivalent thresholds for
855 other common indicators are shown in Figure 3-1. The error is exacerbated by slower indicators and thus

26

856 more accurate measurements of information will result from using the fastest, narrowest kernel
857 indicators available, assuming signal to noise and detection efficiency are comparable across the
858 different width indicators.

859 Guideline 4: We conclude that with careful consideration of the size of the spatial bins in relation to the
860 spatial shift and smoothing induced by the indicator, $\widehat{I_{AP}^F}$ can be used to extract useful measurements of
861 information, most accurately for neurons with < 3 bits/AP under recording conditions similar to those
862 considered here.

863 Previous research quantifying information in bits per AP using $\widehat{I_{AP}^E}$ have found that the majority of
864 neurons carry information in this range (< 3 bits/AP) (Bourboulou et al., 2019; Knierim et al., 1995; Lee
865 et al., 2006; Markus et al., 1995; Poucet and Sargolini, 2013), with a few exceptions (Ji and Wilson,
866 2007). Although these levels are dependent on the number of bins and bin dwell time, $\widehat{I_{AP}^F}$ should be
867 widely applicable to quantifying information throughout the brain during behavior.

868 *Example: application of information metrics to functional fluorescence imaging data from hippocampus*
869 *during spatial behavior*

870 In this section we demonstrate use of the above guidelines for proper application and interpretation of
871 the SMGM fluorescence mutual information metrics ($\widehat{I_S^F}$ and $\widehat{I_{AP}^F}$) defined in Equations 7 and 8. We
872 applied these metrics to functional fluorescence recordings (gCaMP6f) from pyramidal neurons in CA1
873 of the hippocampus acquired during mouse spatial behavior.

874 CA1 neurons expressing gCaMP6f (viral transfection, *Camk2a* promoter) were imaged with two-photon
875 microscopy through a chronic imaging window during mouse navigation along a familiar 1D virtual
876 linear track, as described previously (Figure 5A-B, Dombeck et al., 2010; Radvansky and Dombeck,
877 2018; Sheffield et al., 2017). 8 fields of view from 4 mice were recorded in 8 total sessions (recording
878 duration 8.8+/-1.3 minutes, number of traversals/session: 29+/-2.5, 3.6+/-0.3 laps/min, 3 m long track).
879 From these 8 sessions, 1,500 neurons were identified from our segmentation algorithm (see Methods),
880 and analysis was restricted to the 964 neurons that displayed at least one calcium transient on at least 1/3
881 of the traversals during the session. Among these 964 neurons, 304 (31.5%) had significant place fields
882 and were thus identified as place cells (see Methods), while the remaining 660 (68.5%) did not pass a
883 place field test and were thus identified as non-place cells.

884 By applying Equation 7 (using 5 cm sized spatial bins), we found a continuum of spatial information
885 values measured by the fluorescence SMGM bits per second metric ($\widehat{I_S^F}$) across the 964 CA1 neurons,
886 with an average value of $\widehat{I_S^F}=0.14\pm0.0040 \frac{\text{bits } \Delta F/F}{\text{Hz}}$ (Figure 5C). The units for $\widehat{I_S^F}$ make direct use and
887 interpretation of these values difficult, however, because these recordings were all from pyramidal

27

888 neurons in a single area, here for illustrative purposes, we will presume that variations in c (discussed
889 above) across the 964 neurons of interest are small and acceptable, with the absolute value of c
890 unknown. This allows for comparisons of information ratios across different subsets of the population.
891 For example, place cells had 2.8±0.20 times more information than non-place cells using the SMGM

892 bits per second metric ($\widehat{I_S^F}$=0.18±0.0047 for place vs. 0.063±0.0029 $\frac{\text{bits }\Delta F/F}{\text{Hz}}$ for non-place, Rank sum

893 p=1.7e-63, Figure 5D-F), although there was substantial overlap in information between the populations
894 (see distributions in Figure 5D and individual examples in Figure 5E,F). This also allows for accurate
895 division of the 964 neurons into 3 quantiles based on information values, which we use below for spatial
896 location decoding.

897 By applying Equation 8 (using 5 cm sized spatial bins), we found a continuum of spatial information
898 values measured by the fluorescence SMGM bits per AP metric ($\widehat{I_{AP}^F}$) across the 964 CA1 neurons, with
899 an average value of $\widehat{I_{AP}^F}$=1.65±0.023 bits/AP (Figure 5C). The units for $\widehat{I_{AP}^F}$ allow for direct use and
900 interpretation of these values, and notably, because most (97%) of the neurons had values less than 3
901 bits/AP, a mean absolute error of <10% can be assumed across the distribution of SMGM bits per AP
902 values. When applied to the place and non-place cell populations, we found that place cells had higher
903 information than nonplace cells using the fluorescence SMGM bits per AP metric ($\widehat{I_{AP}^F}$=1.8±0.026 and
904 1.35±0.042 bits/AP, Rank sum p=4.6e-21, Figure 5D-F). This is consistent with mock fluorescence
905 traces generated from real neuron AP datasets (Figure 5-1B).

906 As a demonstration of the usefulness of using information metrics to analyze large functional
907 fluorescence population recordings, we explored the accuracy of decoding the animal's track position
908 using different subsets of neurons. We divided the 964 neurons into 9 groups: All neurons, place cells,
909 non-place cells, three quantiles based on the fluorescence SMGM bits per second metric, and three
910 quantiles based on the fluorescence SMGM bits per AP metric. We then used a Bayesian decoder of the
911 animals' position (see Methods) separately for each of the 9 neuron groups in each of the 8 sessions
912 (Figure 5G,H). An individual session decoding example can be seen in Figure 5G. We quantified
913 decoding accuracy using the absolute position decoding error (% of track), and pooled this measure
914 across sessions for each neuron group (Figure 5H). The means and standard errors for each group are:
915 All neurons (7.33 +/-2.5 %), place cells (6.97 +/-1.9 %), non-place cells (20.9 +/-1.8 %), SMGM bits per
916 second Q1 (21.9 +/-1.5 %), SMGM bits per second Q2 (13.2 +/-2.4 %), SMGM bits per second Q3 (8.97
917 +/-2.4 %), SMGM bits per AP Q1 (17.6 +/-2.7%), SMGM bits per AP Q2 (17.8 +/-3.1 %), SMGM bits
918 per AP Q3 (10.4 +/-3.0 %). Interestingly, even the lowest quantile information groups still could be used
919 to determine animal track location to within ~1/5 of the track. This supports the idea that the
920 hippocampal code for space is carried by a large population of active neurons (Meshulam et al., 2016),
921 and not just by a select subpopulation with the highest information or most well-defined tuning curves.
922 As could be expected, place cells encoded the position of the animal better than nonplace cells and better
923 than the lowest quantile information groups (Holm-Bonferroni corrected Rank sum, α=0.05) and

28

924   neurons in the higher quantiles provided more accurate decoding. Thus, the fluorescence information
925   metrics provide a means to compare the relative contribution of hippocampal neurons with different
926   information values to decoding animal position.

Discussion

928   Here, we performed an in-depth simulation study to examine the application of the SMGM bits per
929   second and SMGM bits per AP metrics of mutual information to functional fluorescence recordings.
930   Since these metrics were designed for AP recordings and since functional fluorescence recordings
931   violate some of the assumptions that these metrics are based on, it was unclear if and how the metrics
932   could be used for functional fluorescence recordings. We created a library of ten thousand mock neurons
933   whose AP output carried ground-truth amounts of information about the animal's spatial location, and
934   by using real behavioral recording data from mice navigating in virtual linear tracks, we simulated the
935   spatial firing patterns of the mock neurons. We then simulated fluorescent calcium responses for each
936   neuron in each session by convolving the AP trains with calcium kernels for different indicators,
937   primarily GCamp6f (though see Figures 2-2 and 3-1 for results from other indicators), and then added
938   noise.

939   We then derived fluorescence versions of the SMGM bits per second ($\widehat{I_S^F}$) and SMGM bits per AP
940   metrics ($\widehat{I_{AP}^F}$) (Equations 7 and 8) and applied them to the fluorescence traces in order to quantify the
941   performance of the metrics for estimating information. We found that ground truth information, as
942   measured by the fluorescence SMGM bits per second metric ($\widehat{I_S^F}$), was transformed into different units
943   and was linearly scaled by a factor (c) dependent on the height and width of the kernel, with c linearly
944   dependent on height and nonlinearly dependent on width. The error induced by these transformations
945   changed substantially over the range of kernel values of the different functional indicators widely used
946   today, and therefore are important factors to consider when designing and interpreting functional
947   imaging experiments. We then found that ground truth information, as measured by the fluorescence
948   SMGM bits per AP metric ($\widehat{I_{AP}^F}$), retains the units and insensitivity to height scaling of the
949   electrophysiological metric ($\widehat{I_{AP}^E}$), but is nonlinearly biased by the smoothing of the fluorescence map
950   dictated by the width of the kernel. The estimation errors strongly depended on both the width of the
951   kernel and the information value being measured. Importantly, since these parameters change
952   substantially over the different functional indicators and different neuron types and behaviors that are
953   commonly used today, they are important factors to consider when designing and interpreting functional
954   imaging experiments. For example, even for the same indicator, the shape of the kernel is a function of
955   intracellular calcium buffering, indicator concentration, the amount of calcium influx, the efflux rates,
956   background fluorescence and resting calcium concentration, which can all vary across different cells.
957   Additionally, the results presented here rely on the approximation that ΔF/F scales linearly with the
958   firing rate, which is not strictly true in practice. We show in Figure 3-3 that even a relatively simple
959   nonlinearity between ΔF/F and firing rate can add distortions to the amount of information measured
960   using the fluorescence SMGM approach. This relationship between ΔF/F and firing rate can vary across

29

961   different indicators and, since the Toolbox can be used to vary this relationship, users can further
962   explore this source of bias.

963   In our approach, the known information values in our library of 10,000 mock neurons were determined
964   using the SMGM metric, which includes the assumption that neuron firing follows an inhomogenous
965   Poisson process. It is important to remember that the SMGM metric, which has been applied to spiking
966   data extensively over the past few decades, *requires* the use of a Poisson estimate of spiking
967   probability—i.e. the Poisson assumption is built into the original metric. In practice, even spiking data
968   violates this and other assumptions of the SMGM metric since real neurons do not strictly follow
969   Poisson statistics (for example they can display neural hysteresis) and animal behavior is non-stationary.
970   Here we are building from this existing framework and adding and testing whether it is possible to apply
971   the metric to functional fluorescence datasets. Even still, the Poisson assumption could have contributed
972   to some of the biases found when evaluating the fluorescence SMGM metrics with respect to ground
973   truth information. We explored this potential source of bias further using two different analyses. First, in
974   Figure 4-2, we applied the Binned Estimators (which do not rely on a Poisson firing assumption) to AP
975   traces and compared the estimated information to the ground truth information (which was established
976   using the SMGM metric that does rely on a Poisson firing assumption). We found the errors to be
977   relatively small, particularly in comparison to the errors induced by the Binned Estimators when applied
978   to fluorescence traces (Figure 4 D,E). Second, in Figure 5-1, we used a real spiking dataset from
979   hippocampal neurons in mice running on a behavioral track (i.e. real spiking neurons that can deviate
980   from Poisson firing) and generated mock fluorescence traces from the AP traces. When we compared
981   the information measured from the AP traces to the fluorescence traces, we found biases that were
982   largely consistent with those observed in Figure 2 and 3 from our simulated mock neuron datasets.
983   Taken together, these analyses indicate that any biases resulting from the Poisson assumption in the
984   simulation procedure appear to be small, particularly with respect to the biases introduced when AP
985   traces are transformed into functional fluorescence traces. Finally, in the Toolbox, we also include code
986   to generate mock neurons using a binned distribution, avoiding the Poisson assumption of SMGM. Thus
987   users can further explore sources of bias using a different ground truth dataset.
988   Using our mock fluorescence traces, we also asked if an AP estimation method could relieve the biases
989   in the SMGM metrics. Applying the SMGM bits per second metric ($\widehat{I_s^d}$) to AP estimation traces from a
990   deconvolution algorithm (FOOPSI) resulted in a low c value for recovered versus ground truth
991   information. When the SMGM bits per AP measure was applied ($\widehat{I_{AP}^d}$), the resulting measurements of
992   information were still nonlinear (compared to $\widehat{I_s^F}$), with a positive bias at lower values of ground truth
993   information. Overall, applying FOOPSI to fluorescence traces led to a poorer recovery of ground truth
994   information using SMGM compared to direct application of SMGM to the florescence traces ($\widehat{I_{AP}^F}$).
995   Importantly, this result from deconvolution is only specific to GCaMP6f, and conclusions should not be
996   drawn about other indicators or situations; users will be able to use the Toolbox to explore this area
997   further. We also tested other metrics to measure mutual information directly from the fluorescence time
998   traces (KSG, Binned Estimator (uniform bins), and Binned Estimator (occupancy binned)) and found

30

999   these alternatives produced highly variable, saturating measurements of recovered versus ground truth
1000   information. This was in contrast to the SMGM bits per second measure ($\widehat{I_S^F}$) which produced a linearly
1001   scaled bias with lower error.

1002   Taken together, we find that the SMGM bits per AP metric can well recover the mutual information
1003   between spiking and behavior. The SMGM bits per second metric is scaled such that comparisons
1004   should be limited to within populations of well characterized neurons or for within neuron comparisons,
1005   e.g. ratios of information across conditions. In general, researchers should use caution when applying
1006   measures developed for AP data in fluorescence recordings: there's no guarantee that the assumptions
1007   that support the measures hold for fluorescence data, and this can lead to difficult to interpret and biased
1008   results.

1009

Figure Captions

1011   <u>Figure 1.</u> Procedures for generating a library of 10,000 neurons with known amounts of information. (A)
1012   Five splines with a gradient of ground truth information (I_{AP}^E) representing the steps in generating a
1013   continuous rate map ($\lambda(x)$) matching the desired target information, in this case 2 bits/AP. Red X's
1014   indicate control nodes that were moved to change the shape of the spline and minimize the squared error
1015   to the target information. (B) Cross section of the error surface around the solution point as a function of
1016   the position of node 3, and the trajectory taken by the solver to minimize the error and arrive at the
1017   target. (C) Histograms of ground truth information resulting from repeating the procedure in A-B 10,000
1018   times to target a range of ground truth information values in bits per second (I_S^E) and bits per AP
1019   (I_{AP}^E).(D) Splines representing $\lambda(x)$ at the solution point for a low (I_{AP}^E=0.04 bits per AP, left) and high
1020   (I_{AP}^E, 2 bits per AP, right) information neuron. (E) Steps to generate mock AP and functional
1021   fluorescence data. (1) An example real behavior trace from a mouse running on a linear track that was
1022   used to generate the simulated spiking. (2) The behavior in combination with the rate maps generated in
1023   A-D were used to generate an instantaneous firing rate trace. (3) The instantaneous rate was used to
1024   pseudorandomly generate APs, as shown in this mock raster. (4) The AP raster was convolved with the
1025   GCaMP6f kernel (red, inset) and noise was added to generate a mock $\frac{\Delta F}{F}$ trace. (5) Large numbers of
1026   these traces were generated and used to assess the effects of many simulation parameters on the
1027   estimators. (F-L) Spiking and fluorescence activity patterns generated from the example simulated
1028   neurons shown in D and using a mean firing rate of 1 Hz. (F) Behavioral trace in blue with AP raster
1029   shown in red. (G) Lap-by-lap raster of the neurons' firing vs mouse track position. (H) Lap by lap
1030   binned, firing rates vs mouse track position for the neurons (I) AP raster (red) and mock calcium traces
1031   for the same behavioral period shown in F. (J) Lap by lap mean binned fluorescence vs mouse position
1032   for the neurons. (K) Binned average firing rate (λ_i, black) and fluorescence intensity (f_i, green) maps for
1033   the two neurons. These maps were used for information analyses.

31

1034

Figure 2. Quantification of the precision of the SMGM bits per second metric using APs or functional fluorescence recordings. (A) Three representative mock neurons spanning the range of ground truth information values in bits per second (I_s^E). From top to bottom for each: mouse track position vs time, AP raster, fluorescence calcium trace (green), and firing rate map (λ_i, black) and change in fluorescence map (f_i, green). (B-D) The ground truth bits per second values are well recovered when measured from AP traces. (B) Information measured from AP data using the SMGM bits per second metric ($\widehat{I_s^E}$) vs ground truth information (I_s^E). Each dot is a single mock neuron, the gray dashed line is the unity line (perfect measurement), the pink line is the line of best fit. Red circles show the examples in A. (C) Percentage error for the information measurements shown in B. (D) Heat map of percentage error measurements shown in C. Black lines are 2 standard deviations, the white line is the mean. (E-G) Effects of applying the SMGM bits per second metric to fluorescence traces. (E) Information measured from mock GCaMP6f traces using the SMGM bits per second metric ($\widehat{I_s^F}$) vs ground truth information (I_s^E). (F) Percentage error for the information measurements shown in E. (G) Heat map of percentage error measurements shown in F. (H) Representative mock kernels mimicking responses from different indicators. (I-K) The effect of kernel height on estimating ground truth information (I_s^E) using the SMGM bits per second metric ($\widehat{I_s^F}$). Kernel height for the kernels shown in H are indicated by colored triangles (I) Percentage error as a function of kernel height (J) Heat map of percentage error measurements shown in I with mean (white) and 2 standard deviations (black). (K) The average percentage error as a function of kernel height and ground truth information in SMGM bits per second (I_s^E). (L-N) The effect of kernel width on estimating ground truth information (I_s^E) using the SMGM bits per second metric ($\widehat{I_s^F}$). Kernel widths for the kernels shown in H are indicated by colored triangles. (L) Percentage error as a function of kernel width (M) Heat map of percentage error measurements shown in L with mean (white) and 2 standard deviations (black). (N) The average percentage error as a function of kernel width. Recording density affected the metrics (Figure 2-1). Changing the kernel to common indicators yielded qualitatively similar, but quantitatively different results (Figure 2-2)

Figure 2-1. Effect of recording density on information metrics. A. The mean error (top) and absolute error (bottom) between the ground truth information (I_s^E) and measured information in SMGM bits per second from mock APs ($\widehat{I_s^E}$) as a function of the mean firing rate ($\bar{\lambda}$). B. As A, but as a function of number of laps. C-D. As A-B, but for measurements from mock fluorescence traces. E-F. As A-B, but for the SMGM bits per AP metric. G-H.) As C-D, but for the SMGM bits per AP metric.

Figure 2-2. Effects of applying the SMGM bits per second metric to fluorescence traces from different common functional indicators. Top: Information measured from mock traces using the SMGM bits per second metric ($\widehat{I_s^F}$) vs ground truth information (I_s^E). Each dot is a single mock neuron, the gray dashed line is the unity line (perfect measurement), the pink line is the line of best fit. Middle: Percentage error

32

1069 density plots. The white line is the mean, the black are $\pm$ one standard deviation. Bottom: Summary
1070 statistics and estimates for the scaling factor c.

1071

1072 <u>Figure 3.</u> Quantification of the precision of the SMGM bits per AP metric using APs or functional
1073 fluorescence recordings. (A) Three representative mock neurons spanning the range of ground truth
1074 information values in bits per AP (I_{AP}^E). From top to bottom for each: mouse track position vs time, AP
1075 raster, fluorescence calcium trace (green), and firing rate map (λ_i, black) and change in fluorescence
1076 map (f_i, green). (B-D) The ground truth bits per AP values are well recovered when measured from AP
1077 traces. (B) Information measured from AP data using the SMGM bits per AP metric ($\widehat{I_{AP}^E}$) vs ground
1078 truth information (I_{AP}^E). Each dot is a single mock neuron, the gray dashed line is the unity line (perfect
1079 measurement). Red circles show the examples in A. (C) Percentage error for the information
1080 measurements shown in B. (D) Heat map of percentage error measurements shown in C. Black lines are
1081 2 standard deviations, the white line is the mean. (E-G) Effects of applying the SMGM bits per AP
1082 metric to fluorescence traces. (E) Information measured from mock GCaMP6f traces using the SMGM
1083 bits per AP metric ($\widehat{I_{AP}^F}$) vs ground truth information (I_{AP}^E). (F) Percentage error for the information
1084 measurements shown in E. (G) Heat map of percentage error measurements shown in F. (H-J) The effect
1085 of kernel height on estimating ground truth information (I_{AP}^E) using the SMGM bits per second metric
1086 ($\widehat{I_{AP}^F}$). Kernel height for the kernels shown in Figure2H are indicated by colored triangles (H) Percentage
1087 error as a function of kernel height (I) Heat map of percentage error measurements shown in H with
1088 mean (white) and 2 standard deviations (black). (J) The average percentage error as a function of kernel
1089 height and ground truth information in bits per AP (I_{AP}^E). (K-M) The effect of kernel width on estimating
1090 ground truth information (I_{AP}^E) using the SMGM bits per AP metric ($\widehat{I_{AP}^F}$). Kernel widths for the kernels
1091 shown in Figure 2H are indicated by colored triangles. (L) Percentage error as a function of kernel width
1092 (M) Heat map of percentage error measurements shown in L with mean (white) and 2 standard
1093 deviations (black). (N) The average percentage error as a function of kernel width. Changing the kernel
1094 to common indicators yielded qualitatively similar, but quantitatively different results (Figure 3-1).
1095 These errors could not be resolved by changing the bin width (Figure 3-2). Addition of a nonlinearity
1096 further distorted the measured information (Figure 3-3).

1097 <u>Figure 3-1.</u> Effects of applying the SMGM bits per AP metric to fluorescence traces from different
1098 common functional indicators. Top: Information measured from mock traces using the SMGM bits per
1099 AP metric ($\widehat{I_{AP}^F}$) vs ground truth information (I_{AP}^E). Each dot is a single mock neuron, the gray dashed
1100 line is the unity line (perfect measurement), the pink line is the exponential fit. Middle: Percentage error
1101 density plots. The white line is the mean, the black are $\pm$ one standard deviation. Bottom: Summary
1102 statistics and percent error cutoffs.

33

1103   <u>Figure 3-2.</u> Effect of number of bins on the SMGM metrics. A. The mean percentage error (top) and the
1104   standard deviation (bottom) for the bits per second measure ($\widehat{I_S^F}$) applied to 10,000 mock gCamp6f
1105   traces, with ground truth information on the X-axis and 2-60 bins (3m track) on the Y-axis. B. As A, for
1106   the bits per AP measure ($\widehat{I_{AP}^F}$). C. The mean percentage error (top) and the standard deviation (bottom)
1107   for the bits per second measure ($\widehat{I_S^F}$) applied to 20,000 mock fluorescence traces with differing kernel
1108   width. Kernel width is on the X-axis, number of bins is on the Y-axis. D. As C, but for the bits per AP
1109   measure ($\widehat{I_{AP}^F}$).

1110   <u>Figure 3-3.</u> Effects of a sigmoid nonlinearity between ΔF/F and firing rate. Here we applied a log-
1111   sigmoid nonlinearity to the 10,000 mock GCaMP6f time-series traces and then measured information
1112   using the fluorescence SMGM metrics. (A) Nonlinearity applied to AP-to-florescence trace
1113   transformation (B) Information measured from AP data using the SMGM bits per second ($\widehat{I_S^F}$) vs ground
1114   truth information (I_S^E). Each dot is a single mock neuron, the gray dashed line is the unity line (perfect
1115   measurement). (C) Percentage error for the information measurements shown in B. (D) Heat map of
1116   percentage error measurements shown in C. Black lines are 2 standard deviations, the white line is the
1117   mean. (E-G) As B-D, but for the bits per AP measured ($\widehat{I_{AP}^F}$) versus the ground truth information in bits
1118   per AP (I_{AP}^E).

1119

1120   <u>Figure 4.</u> Alternative techniques for measuring mutual information from functional fluorescence traces.
1121   (A-E) (Top) Information measured from mock GCaMP6f traces vs ground truth information. The gray
1122   line is the unity line, the pink line is the best fit saturating exponential. (Middle) Percentage error for the
1123   information measurements shown on top. (Bottom) Heat map of percentage error measurements shown
1124   in middle. (A) FOOPSI deconvolved traces using the SMGM bits per second metric ($\widehat{I_S^d}$). (B) FOOPSI
1125   deconvolved traces using the SMGM bits per AP metric ($\widehat{I_{AP}^d}$). The regularization coefficient had little
1126   effect on these results (Figure 4-1). (C) The KSG measure applied to GCaMP6f traces. (D) The Binned
1127   Estimator applied to GCaMP6f traces using uniform bins. (E) The Binned Estimator applied to
1128   GCaMP6f traces using equal occupancy bins. The binned estimators were less distorted on the raw AP
1129   traces (Figure 4-2). (F) Table of summary statistics for each measure. P exponential is the p-value from
1130   the chi^2 test used to determine if a saturating exponential fit is better than a linear fit for the measured vs
1131   ground truth information plots. An analytic solution yielded qualitatively similar, but quantitatively
1132   disparate results (Figure 4-3).

1133   <u>Figure 4-1.</u> Effect of changing the regularization coefficient in deconvolution (Friedrich et al., 2017;
1134   Vogelstein et al., 2010) on the measured information. (A) The measured information using the
1135   fluorescence bits per second metric applied to 10,000 mock GCaMP6f traces using regularization
1136   coefficients between 0 and 3. (B) As A, but for the fluorescence bits per AP metric.

   34

1137 <u>Figure 4-2.</u> The binned estimator applied to AP traces and then compared to ground truth information.
1138 (Top) Information measured from mock AP traces vs ground truth information. The gray line is the
1139 unity line, the pink line is the best fit saturating exponential. (Middle) Percentage error for the
1140 information measurements shown on top (same scale as shown in Figure 4). (Bottom) Heat map of
1141 percentage error measurements shown in middle. (A) The Binned Estimator applied to AP traces using
1142 uniform bins. (B) The Binned Estimator applied to AP traces using equal occupancy bins.

1143 <u>Figure 4-3.</u> Information for neurons with Gaussian rate maps. (A) Blue: Information measured from
1144 mock GCaMP6f traces using the SMGM bits per second metric ($\widehat{I_s^F}$) vs ground truth information (I_s^E).
1145 Red: Information approximated using the analytic approximation in Equation 9. Each dot is a single
1146 mock neuron with a Gaussian rate map. The gray dashed line is the unity line (perfect measurement).
1147 (B) Percentage error for the information measurements shown in A. (C) Blue: Information measured
1148 from mock GCaMP6f traces using the SMGM bits per AP metric ($\widehat{I_{AP}^F}$) vs ground truth information
1149 (I_{AP}^E). Red: Information approximated using the analytic approximation in Equation 10. Each dot is a
1150 single mock neuron with a Gaussian rate map. The gray dashed line is the unity line (perfect
1151 measurement). (D) Percentage error for the information measurements shown in C.

1152 <u>Figure 5.</u> Application of SMGM information metrics to functional fluorescence imaging data from
1153 hippocampus during spatial behavior. A.) Example field of hippocampal pyramidal neurons expressing
1154 GCaMP6f and imaged during linear track navigation. Active cell ROIs shown in yellow; traces for green
1155 cells shown in B. B.) Fluorescence DF/F traces (green) from two neurons in the field shown in A and the
1156 track position during the recording (blue). C.). Distribution of information values using the fluorescence
1157 SMGM bits per second metric ($\widehat{I_s^F}$,(top) and the fluorescence SMGM bits per AP metric ($\widehat{I_{AP}^F}$, bottom).
1158 The gray line indicates the recommended cutoff for reliability using GCaMP6f. D.) Plot of $\widehat{I_s^F}$ vs $\widehat{I_{AP}^F}$ for
1159 each neuron. Place cells indicated in red and nonplace cells in blue. E.) Example non-place cells
1160 spanning the information ranges shown in C. Spatial fluorescence map (f_i) shown on left, and average
1161 change in fluorescence per track traversal on right. F.) Same as E, but for place cells. G.) Bayesian
1162 decoding of mouse's track position using different subpopulations of neurons for one example session.
1163 From top to bottom: All active neurons, all nonplace cells, and place cells, the first through third
1164 quantiles of the SMGM bits per second formulation ($\widehat{I_s^F}$), and the first through third quantiles of the
1165 SMGM bits per AP formation ($\widehat{I_{AP}^F}$). The white dashed line indicates the ground truth position of the
1166 animal, the color map indicates the decoded position probability (peak-normalized posterior
1167 distribution). H.) Decoding accuracy (absolute position decoding error in units of % of track) pooled
1168 over all sessions for each neuron group indicated in G. Black bars indicate significant differences by
1169 Holm-Bonferroni corrected rank sum tests (α=0.05). Consistent results were obtained when measuring
1170 information from real spiking data and simulated florescence traces. (Figure 5-1).

1171 <u>Figure 5-1.</u> The SMGM estimators as applied to real AP data from a real spiking dataset from
1172 hippocampal neurons in mice running on a behavioral track (Chen et al., 2016; Grosmark and Buzsaki,

35

1173 2016; Grossmark et al., 2016). (A) Example real place cell. From top to bottom: rat track position vs
1174 time, real AP raster, mock fluorescence calcium trace generated from real AP trace by convolving APs
1175 with GCaMP6f kernel and adding noise (green), and firing rate map (λ_i, black) and change in mock
1176 fluorescence map (f_i, green). (B)Plot of $\widehat{I_S^F}$ vs $\widehat{I_{AP}^F}$ for each neuron. Place cells indicated in red and
1177 nonplace cells in blue. (C) The SMGM bits per second metric applied to the real AP traces ($\widehat{I_S^E}$) versus
1178 the mock fluorescence traces ($\widehat{I_S^F}$) (generated from the real AP traces). (D) The percentage difference
1179 between the SMGM bits per second metric applied to the real AP traces ($\widehat{I_S^E}$) and the mock fluorescence
1180 traces ($\widehat{I_S^F}$). The mean and standard deviation are indicated in black. In magenta, the mean and standard
1181 deviation of 5,000 of the mock neuron traces seen in Figures 2 and 3, sampled to have the same firing
1182 rates as the real neurons and shortened to the same mean session duration. (E) Density plot for the data
1183 shown in D. (F-H) As C-E, but for the bits per AP metric ($\widehat{I_{AP}^E}$ versus $\widehat{I_{AP}^F}$).

1184

1185

References

1187 Ahrens MB, Orger MB, Robson DN, Li JM, Keller PJ. 2013. Whole-brain functional imaging at cellular
1188   resolution using light-sheet microscopy. *Nat Methods* **10**:413–420. doi:10.1038/nmeth.2434

1189 Allen TA, Salz DM, McKenzie S, Fortin NJ. 2016. Nonspatial Sequence Coding in CA1 Neurons. *J*
1190   *Neurosci* **36**:1547–1563. doi:10.1523/JNEUROSCI.2874-15.2016

1191 Aponte Y, Bischofberger J, Jonas P. 2008. Efficient Ca2+ buffering in fast-spiking basket cells of rat
1192   hippocampus. *J Physiol* **586**:2061–2075. doi:10.1113/jphysiol.2007.147298

1193 Aronov D, Tank DW. 2014. Engagement of Neural Circuits Underlying 2D Spatial Navigation in a
1194   Rodent Virtual Reality System. *Neuron* **84**:442–456. doi:10.1016/j.neuron.2014.08.042

1195 Belghazi MI, Baratin A, Rajeswar S, Ozair S, Bengio Y, Courville A, Hjelm RD. 2018. MINE: Mutual
1196   Information Neural Estimation. *35th Int Conf Mach Learn ICML 2018* **2**:864–873.

1197 Bourboulou R, Marti G, Michon FX, El Feghaly E, Nouguier M, Robbe D, Koenig J, Epsztein J. 2019.
1198   Dynamic control of hippocampal spatial coding resolution by local visual cues. *Elife* **8**:1–30.
1199   doi:10.7554/eLife.44487

1200 Brandon MP, Bogaard AR, Libby CP, Connerney MA, Gupta K, Hasselmo ME. 2011. Reduction of
1201   Theta Rhythm Dissociates Grid Cell Spatial Periodicity from Directional Tuning. *Science (80-)*
1202   **332**:595–599. doi:10.1126/science.1201652

1203 Brown EN, Barbieri R, Eden UT, Frank L. 2003. Likelihood Methods for Neural Spike Train Data
1204   Analysis In: Feng J, editor. Computational Neuroscience: A Comprehensive Approach. CRC Pres.
1205   pp. 252–281.

1206 Buzsáki G, Mizuseki K. 2014. The log-dynamic brain: how skewed distributions affect network
1207   operations. *Nat Rev Neurosci* **15**:264–78. doi:10.1038/nrn3687

1208 Calton JL, Stackman RW, Goodridge JP, Archey WB, Dudchenko PA, Taube JS. 2003. Hippocampal
1209   place cell instability after lesions of the head direction cell network. *J Neurosci* **23**:9719–9731.
1210   doi:23/30/9719 [pii]

1211 Chen Q, Cichon J, Wang W, Qiu L, Lee SJR, Campbell NR, DeStefino N, Goard MJ, Fu Z, Yasuda R,
1212   Looger LL, Arenkiel BR, Gan WB, Feng G. 2012. Imaging Neural Activity Using Thy1-GCaMP
1213   Transgenic Mice. *Neuron* **76**:297–308. doi:10.1016/j.neuron.2012.07.011

1214 Chen T-W, Wardill TJ, Sun Y, Pulver SR, Renninger SL, Baohan A, Schreiter ER, Kerr RA, Orger MB,
1215   Jayaraman V, Looger LL, Svoboda K, Kim DS. 2013. Ultrasensitive fluorescent proteins for
1216   imaging neuronal activity. *Nature* **499**:295–300. doi:10.1038/nature12354

1217 Chen Z, Grosmark AD, Penagos H, Wilson MA. 2016. Uncovering representations of sleep-associated
1218   hippocampal ensemble spike activity. *Sci Rep* **6**:32193. doi:10.1038/srep32193

1219 Climer JR, DiTullio R, Newman EL, Hasselmo ME, Eden UT. 2015. Examination of rhythmicity of
1220   extracellularly recorded neurons in the entorhinal cortex. *Hippocampus* **25**:460–473.
1221   doi:10.1002/hipo.22383

1222 Climer JR, Newman EL, Hasselmo ME. 2013. Phase coding by grid cells in unconstrained
1223   environments: two-dimensional phase precession. *Eur J Neurosci* **38**:2526–41.
1224   doi:10.1111/ejn.12256

1225 Cohen MR, Kohn A. 2011. Measuring and interpreting neuronal correlations. *Nat Neurosci* **14**:811–819.
1226   doi:10.1038/nn.2842

1227 Dana H, Sun Y, Mohar B, Hulse B, Hasseman JP, Tsegaye G, Tsang A, Wong A, Patel R, Macklin JJ,
1228   Chen Y, Konnerth A, Jayaraman V, Looger LL, Schreiter ER, Svoboda K, Kim DS, Hod Dana, Yi
1229   Sun, Boaz Mohar, Brad Hulse, Jeremy P Hasseman, Getahun Tsegaye, Arthur Tsang, Allan Wong,
1230   Ronak Patel, John J Macklin, Yang Chen, Arthur Konnerth, Vivek Jayaraman, Loren L Looger,
1231   Eric R Schreiter, Karel Svoboda DSK. 2018. High-performance GFP-based calcium indicators for
1232   imaging activity in neuronal populations and microcompartments. *bioRxiv* **16**:434589.
1233   doi:10.1101/434589

37

1234   Dana H, Sun Y, Mohar B, Hulse BK, Kerlin AM, Hasseman JP, Tsegaye G, Tsang A, Wong A, Patel R,
1235   Macklin JJ, Chen Y, Konnerth A, Jayaraman V, Looger LL, Schreiter ER, Svoboda K, Kim DS.
1236   2019. High-performance calcium sensors for imaging activity in neuronal populations and
1237   microcompartments. *Nat Methods* **16**:649–657. doi:10.1038/s41592-019-0435-6

1238   DeWeese MR, Zador AM, Hromádka T. 2008. Sparse Representation of Sounds in the Unanesthetized
1239   Auditory Cortex. *PLoS Biol* **6**:14. doi:10.1371/journal.pbio.Citation

1240   Dombeck DA, Harvey CD, Tian L, Looger LL, Tank DW. 2010. Functional imaging of hippocampal
1241   place cells at cellular resolution during virtual navigation. *Nat Neurosci* **13**. doi:10.1038/nn.2648

1242   Dombeck DA, Khabbaz AN, Collman F, Adelman TL, Tank DW. 2007. Imaging large-scale neural
1243   activity with cellular resolution in awake, mobile mice. *Neuron* **56**:43–57.
1244   doi:10.1016/j.neuron.2007.08.003

1245   Éltes T, Szoboszlay M, Kerti-Szigeti K, Nusser Z. 2019. Improved spike inference accuracy by
1246   estimating the peak amplitude of unitary [Ca 2+] transients in weakly GCaMP6f-expressing
1247   hippocampal pyramidal cells. *J Physiol* **597**:2925–2947. doi:10.1113/JP277681

1248   Evans MH, Petersen RS, Humphries MD. 2019. On the use of calcium deconvolution algorithms in
1249   practical contexts. *bioRxiv* 871137. doi:10.1101/871137

1250   Frank LM, Brown EN, Wilson MA. 2001. A comparison of the firing properties of putative excitatory
1251   and inhibitory neurons from CA1 and the entorhinal cortex. *J Neurophysiol* **86**:2029–2040.

1252   Friedrich J, Zhou P, Paninski L. 2017. Fast online deconvolution of calcium imaging data. *PLOS
1253   Comput Biol* **13**:e1005423. doi:10.1371/journal.pcbi.1005423

1254   Fu H, Rodriguez GA, Herman M, Emrani S, Nahmani E, Barrett G, Figueroa HY, Goldberg E, Hussaini
1255   SA, Duff KE. 2017. Tau Pathology Induces Excitatory Neuron Loss, Grid Cell Dysfunction, and
1256   Spatial Memory Deficits Reminiscent of Early Alzheimer's Disease. *Neuron* **93**:533-541.e5.
1257   doi:10.1016/j.neuron.2016.12.023

1258   Fyhn M, Molden S, Hollup S, Moser M-B, Moser EI. 2002. Hippocampal Neurons Responding to First-
1259   Time Dislocation of a Target Object. *Neuron* **35**:555–566. doi:10.1016/S0896-6273(02)00784-5

1260   Gao W, Kannan S, Oh S, Viswanath P. 2017. Estimating mutual information for discrete-continuous
1261   mixturesAdvances in Neural Information Processing Systems. pp. 5987–5998.

1262   Gerrard JL, Burke SN, McNaughton BL, Barnes CA. 2008. Sequence Reactivation in the Hippocampus
1263   Is Impaired in Aged Rats. *J Neurosci* **28**:7883–7890. doi:10.1523/JNEUROSCI.1265-08.2008

38

1264   Greenberg DS, Wallace DJ, Voit K-M, Wuertenberger S, Czubayko U, Monsees A, Handa T,
1265   Vogelstein JT, Seifert R, Groemping Y, Kerr JN. 2018. Accurate action potential inference from a
1266   calcium sensor protein through biophysical modeling. *bioRxiv* 479055. doi:10.1101/479055

1267   Grosmark AD, Buzsaki G. 2016. Diversity in neural firing dynamics supports both rigid and learned
1268   hippocampal sequences. *Science (80-)* **351**:1440–1443. doi:10.1126/science.aad1935

1269   Grossmark AD, Long J, Buzsáki G. 2016. Recordings from hippocampal area CA1, PRE, during and
1270   POST novel spatial learning. doi:dx.doi.org/10.6080/K0862DC5

1271   Grubb MS, Thompson ID. 2006. Quantitative Characterization of Visual Response Properties in the
1272   Mouse Dorsal Lateral Geniculate Nucleus. *J Neurophysiol* **90**:3594–3607.
1273   doi:10.1152/jn.00699.2003

1274   Hainmueller T, Bartos M. 2018. Parallel emergence of stable and dynamic memory engrams in the
1275   hippocampus. *Nature* **558**:292–296. doi:10.1038/s41586-018-0191-2

1276   Harvey CD, Collman F, Dombeck DA, Tank DW. 2009. Intracellular dynamics of hippocampal place
1277   cells during virtual navigation. *Nature* **461**:941–946. doi:nature08499 [pii]10.1038/nature08499

1278   Hazama Y, Tamura R. 2019. Effects of self-locomotion on the activity of place cells in the hippocampus
1279   of a freely behaving monkey. *Neurosci Lett* **701**:32–37. doi:10.1016/j.neulet.2019.02.009

1280   Helmchen F, Tank DW. 2015. A single-compartment model of calcium dynamics in nerve terminals and
1281   dendrites. *Cold Spring Harb Protoc* **2015**:155–167. doi:10.1101/pdb.top085910

1282   Heys JG, Dombeck DA. 2018. Evidence for a subcircuit in medial entorhinal cortex representing
1283   elapsed time during immobility. *Nat Neurosci* **21**:1574–1582. doi:10.1038/s41593-018-0252-8

1284   Heys JG, Rangarajan K V., Dombeck DA. 2014. The functional micro-organization of grid cells
1285   revealed by cellular-resolution imaging. *Neuron* **84**:1079–1090. doi:10.1016/j.neuron.2014.10.048

1286   Hinman JR, Brandon MP, Climer JR, Chapman GW, Hasselmo ME. 2016. Multiple Running Speed
1287   Signals in Medial Entorhinal Cortex. *Neuron* **91**:666–679. doi:10.1016/j.neuron.2016.06.027

1288   Hok V, Chah E, Save E, Poucet B. 2013. Prefrontal Cortex Focally Modulates Hippocampal Place Cell
1289   Firing Patterns. *J Neurosci* **33**:3443–3451. doi:10.1523/JNEUROSCI.3427-12.2013

1290   Huang Y, Brandon MP, Griffin AL, Hasselmo ME, Eden UT. 2009. Decoding movement trajectories
1291   through a T-maze using point process filters applied to place field data from rat hippocampal region
1292   CA1. *Neural Comput* **21**:3305–3334. doi:10.1162/neco.2009.10-08-893

39

1293   Hubel DH, Wiesel TN. 2009. Republication of The Journal of Physiology (1959) 148, 574-591:
1294   Receptive fields of single neurones in the cat's striate cortex. 1959. *J Physiol* **587**:2721–32.
1295   doi:10.1113/jphysiol.2009.174151

1296   Ji D, Wilson MA. 2007. Coordinated memory replay in the visual cortex and hippocampus during sleep.
1297   *Nat Neurosci* **10**:100–107. doi:10.1038/nn1825

1298   Jiaying Tang SS. 2015. Visual receptive field properties of neurons in the mouse LGN. *PLoS Comput*
1299   *Biol* **18**:449–452. doi:10.5061/dryad.b2t22

1300   Jing M, Zhang P, Wang G, Feng J, Mesik L, Zeng J, Jiang H, Wang S, Looby JC, Guagliardo NA,
1301   Langma LW, Lu J, Zuo Y, Talmage DA, Role LW, Barrett PQ, Zhang LI, Luo M, Song Y, Zhu JJ,
1302   Li Y. 2018a. Dendritic Inhibition in the Hippocampus Supports Fear Learning. *Nat Biotechnol*
1303   **36**:726–737. doi:10.1126/science.1247485

1304   Jing M, Zhang P, Wang G, Feng J, Mesik L, Zeng J, Jiang H, Wang S, Looby JC, Guagliardo NA,
1305   Langma LW, Lu J, Zuo Y, Talmage DA, Role LW, Barrett PQ, Zhang LI, Luo M, Song Y, Zhu JJ,
1306   Li Y. 2018b. State-Dependent Subnetworks of Parvalbumin-Expressing Interneurons in Neocortex.
1307   *Nat Biotechnol* **36**:726–737. doi:10.1016/j.celrep.2019.02.005

1308   Jing M, Zhang P, Wang G, Feng J, Mesik L, Zeng J, Jiang H, Wang S, Looby JC, Guagliardo NA,
1309   Langma LW, Lu J, Zuo Y, Talmage DA, Role LW, Barrett PQ, Zhang LI, Luo M, Song Y, Zhu JJ,
1310   Li Y. 2018c. Calcium Dynamics in Dendrites of Hippocampal CA1 Interneurons in Awake Mice.
1311   *Nat Biotechnol* **36**:726–737. doi:10.3389/fncel.2019.00098

1312   Jing M, Zhang P, Wang G, Feng J, Mesik L, Zeng J, Jiang H, Wang S, Looby JC, Guagliardo NA,
1313   Langma LW, Lu J, Zuo Y, Talmage DA, Role LW, Barrett PQ, Zhang LI, Luo M, Song Y, Zhu JJ,
1314   Li Y. 2018d. A genetically encoded fluorescent acetylcholine indicator for in vitro and in vivo
1315   studies. *Nat Biotechnol* **36**:726–737. doi:10.1038/nbt.4184

1316   Kalko EK V, Dukas R, Ratcliffe JM, Teeling EC, Haven N, Fattu JM, Bates ME, Simmons J a,
1317   Riquimaroux H, Surlykke A, Bouffard FH, Lee DN, Dear SP, Horiuchi TK, Krishnaprasad PS,
1318   Moss CF, Schuller G, Brudzynski SM, Syme D a, Hollingworth S, Lindstedt SL, Baylor SM, Mead
1319   a F, Rome LC, Goller F, Spiers ILY, Leeuwen JL Van, Schachat F, Rossmanith GH, Hoh JFY,
1320   Kelley DB, Vater M a, Zhao Y, Araki S, Wu J, Teramoto T, Chang Y-F, Nakano M, Abdelfattah
1321   AS, Fujiwara M, Ishihara T, Nagai T, Campbell RE. 2011. An Expanded Palette of Genetically
1322   Encoded Ca2+ Indicators. *Science (80-)* **333**:1888–1891. doi:10.1126/science.1208592

1323   Keller PJ, Ahrens MB. 2015. Visualizing whole-brain activity and development at the single-cell level
1324   using light-sheet microscopy. *Neuron* **85**:462–483. doi:10.1016/j.neuron.2014.12.039

40

1325   Khoshkhoo S, Vogt D, Sohal VS. 2017. Dynamic, Cell-Type-Specific Roles for GABAergic
1326   Interneurons in a Mouse Model of Optogenetically Inducible Seizures. *Neuron*.
1327   doi:10.1016/j.neuron.2016.11.043

1328   Kinsky NR, Sullivan DW, Mau W, Hasselmo ME, Eichenbaum HB. 2018. Hippocampal Place Fields
1329   Maintain a Coherent and Flexible Map across Long Timescales. *Curr Biol* **28**:3578-3588.e6.
1330   doi:10.1016/j.cub.2018.09.037

1331   Knierim JJ, Kudrimoti HS, McNaughton BL. 1995. Place cells, head direction cells, and the learning of
1332   landmark stability. *J Neurosci* **15**:1648–1659.

1333   Koenig J, Linder AN, Leutgeb JK, Leutgeb S. 2011. The Spatial Periodicity of Grid Cells Is Not
1334   Sustained During Reduced Theta Oscillations. *Science (80-)* **332**:592–595.
1335   doi:10.1126/science.1201685

1336   Kraskov A, Stögbauer H, Grassberger P. 2004. Estimating mutual information. *Phys Rev E - Stat
1337   Physics, Plasmas, Fluids, Relat Interdiscip Top* **69**:16. doi:10.1103/PhysRevE.69.066138

1338   Kraus BJ, Brandon MP, Robinson RJ, Connerney MA, Hasselmo ME, Eichenbaum HB. 2015. During
1339   Running in Place, Grid Cells Integrate Elapsed Time and Distance Run. *Neuron* **88**:578–589.
1340   doi:10.1016/j.neuron.2015.09.031

1341   Kropff E, Carmichael JE, Moser M-B, Moser EI. 2015. Speed cells in the medial entorhinal cortex.
1342   *Nature* **523**:419–424. doi:10.1038/nature14622

1343   Lee I, Griffin AL, Zilli EA, Eichenbaum HB, Hasselmo ME. 2006. Gradual translocation of spatial
1344   correlates of neuronal firing in the hippocampus toward prospective reward locations. *Neuron*
1345   **51**:639–650.

1346   Leveteau J, MacLeod P. 1966. Olfactory discrimination in the rabbit olfactory glomerulus. *Science*
1347   **153**:175–6. doi:10.1126/science.153.3732.175

1348   Liu P, Jerrard LE, Bilkey DK, Jarrard LE, Bilkey DK. 2004. Excitotoxic lesions of the pre- and
1349   parasubiculum disrupt the place fields of hippocampal pyramidal cells. *Hippocampus* **14**:107–116.
1350   doi:10.1002/hipo.10161

1351   MacDonald CJ, Carrow S, Place R, Eichenbaum HB. 2013. Distinct hippocampal time cell sequences
1352   represent odor memories in immobilized rats. *J Neurosci* **33**:14607–16.
1353   doi:10.1523/JNEUROSCI.1537-13.2013

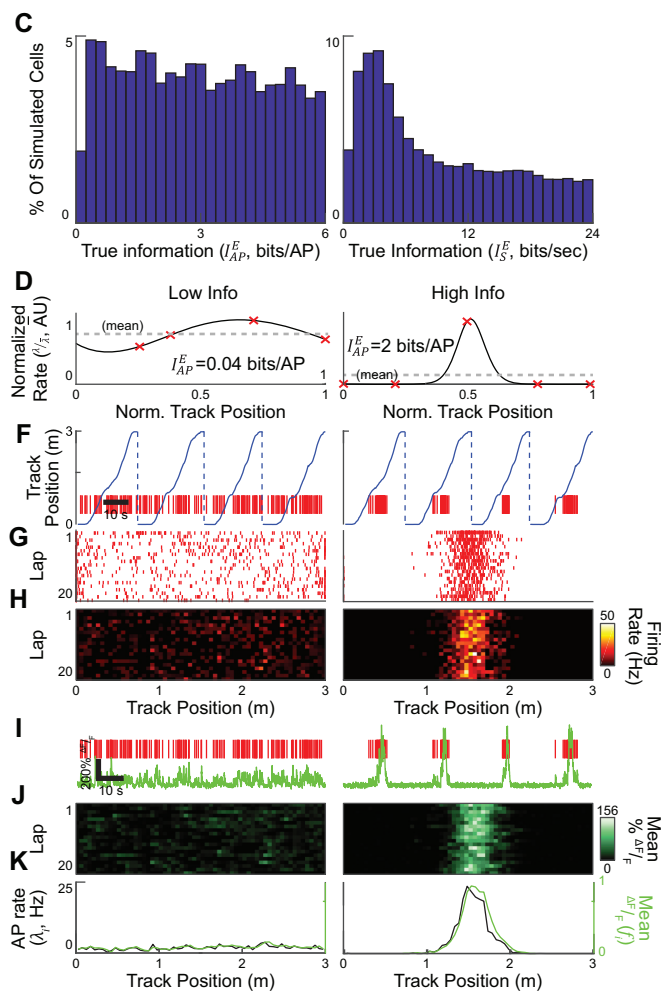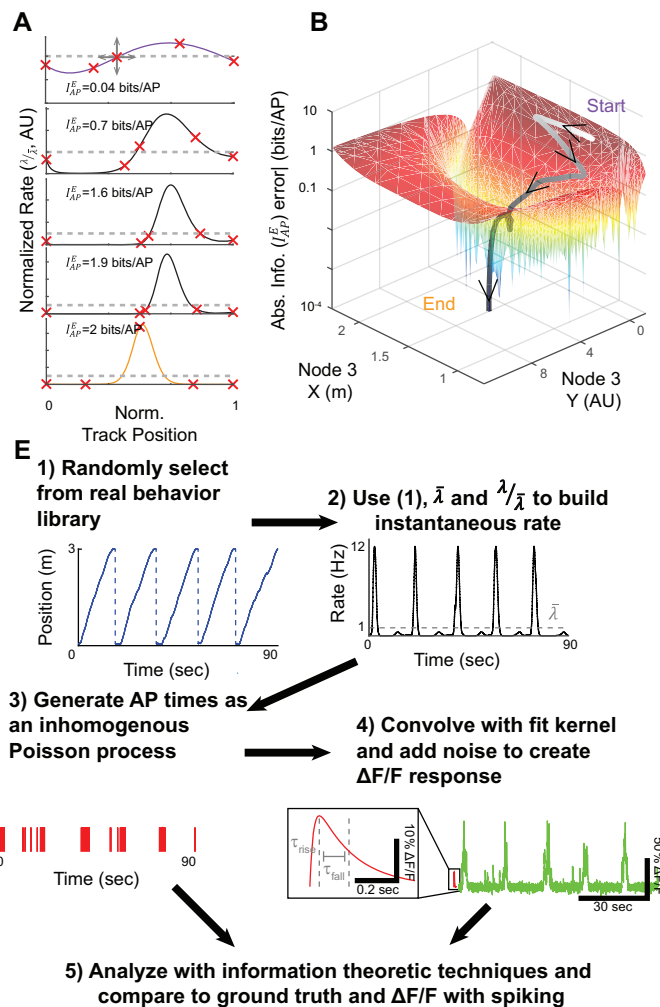1354   Mankin EA, Thurley K, Chenani A, Haas O V, Debs L, Henke J, Galinato M, Leutgeb JK, Leutgeb S,

41

1355   Leibold C. 2019. The hippocampal code for space in Mongolian gerbils. *Hippocampus* 1–15.
1356   doi:10.1002/hipo.23075

1357   Mann K, Gallen CL, Clandinin TR. 2017. Whole-Brain Calcium Imaging Reveals an Intrinsic
1358   Functional Network in Drosophila. *Curr Biol* **27**:2389-2396.e4. doi:10.1016/j.cub.2017.06.076

1359   Markus EJ, Qin YL, Leonard B, Skaggs WEW, McNaughton BBL, Barnes CA. 1995. Interactions
1360   between location and task affect the spatial and directional firing of hippocampal neurons. *J*
1361   *Neurosci* **15**:7079–7094. doi:20026608

1362   Marvin JS, Scholl B, Wilson DE, Podgorski K, Kazemipour A, Müller JA, Schoch S, Quiroz FJU,
1363   Rebola N, Bao H, Little JP, Tkachuk AN, Cai E, Hantman AW, Wang SSH, DePiero VJ, Borghuis
1364   BG, Chapman ER, Dietrich D, DiGregorio DA, Fitzpatrick D, Looger LL. 2018. Stability, affinity,
1365   and chromatic variants of the glutamate sensor iGluSnFR. *Nat Methods* **15**:936–939.
1366   doi:10.1038/s41592-018-0171-3

1367   Marvin JS, Shimoda Y, Magloire V, Leite M, Kawashima T, Jensen TP, Kolb I, Knott EL, Novak O,
1368   Podgorski K, Leidenheimer NJ, Rusakov DA, Ahrens MB, Kullmann DM, Looger LL, Malgoire V,
1369   Leite M, Kawashima T, Jensen TP, Knott EL, Novak O, Podgorski K, Leidenheimer NJ, Rusakov
1370   DA, Ahrens MB, Kullmann DM, Looger LL. 2019. A genetically encoded fluorescent sensor for in
1371   vivo imaging of GABA. *Nat Methods* **16**:763–770. doi:10.1038/s41592-019-0471-2

1372   Mau W, Sullivan DW, Kinsky NR, Hasselmo ME, Howard MW, Eichenbaum H. 2018. The Same
1373   Hippocampal CA1 Population Simultaneously Codes Temporal Information over Multiple
1374   Timescales. *Curr Biol* **28**:1499-1508.e4. doi:10.1016/j.cub.2018.03.051

1375   Meshulam L, Gauthier JL, Brody CD, Tank DW, Bialek W. 2016. Collective behavior of place and non-
1376   place neurons in the hippocampal network 1–17.

1377   Miri A, Daie K, Burdine RD, Aksay E, Tank DW. 2011. Regression-Based Identification of Behavior-
1378   Encoding Neurons During Large-Scale Optical Imaging of Neural Activity at Cellular Resolution. *J*
1379   *Neurophysiol* **105**:964–980. doi:10.1152/jn.00702.2010

1380   Morris TP, White IR, Crowther MJ. 2019. Using simulation studies to evaluate statistical methods. *Stat*
1381   *Med* **38**:2074–2102. doi:10.1002/sim.8086

1382   Mukamel EA, Nimmerjahn A, Schnitzer MJ. 2009. Automated Analysis of Cellular Signals from Large-
1383   Scale Calcium Imaging Data. *Neuron* **63**:747–760. doi:10.1016/j.neuron.2009.08.009

1384   Newman EL, Climer JR, Hasselmo ME. 2014. Grid cell spatial tuning reduced following systemic
1385   muscarinic receptor blockade. *Hippocampus* **24**:643–655. doi:10.1002/hipo.22253
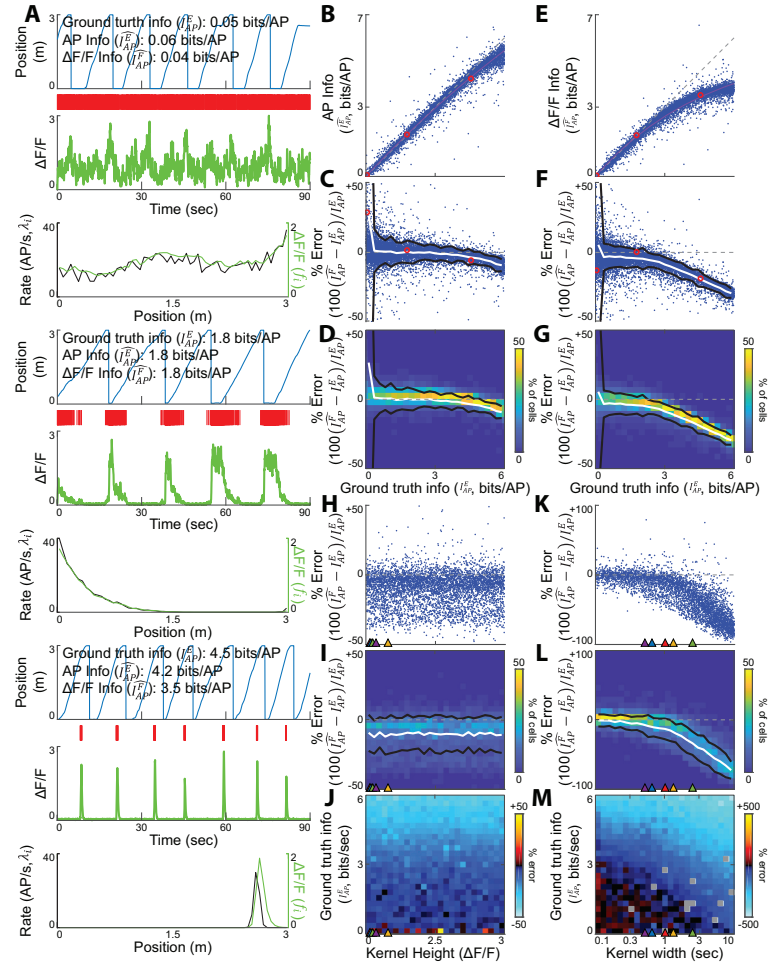
42

1386　Nguyen JP, Shipley FB, Linder AN, Plummer GS, Liu M, Setru SU, Shaevitz JW, Leifer AM. 2016.
1387　　　Whole-brain calcium imaging with cellular resolution in freely behaving Caenorhabditis elegans .
1388　　　*Proc Natl Acad Sci* **113**:E1074–E1081. doi:10.1073/pnas.1507110112

1389　Nguyen MN, Hori E, Matsumoto J, Tran AH, Ono T, Nishijo H. 2013. Neuronal responses to face-like
1390　　　stimuli in the monkey pulvinar. *Eur J Neurosci* **37**:35–51. doi:10.1111/ejn.12020

1391　Nguyen MN, Matsumoto J, Hori E, Maior RS, Tomaz C, Tran AH, Ono T, Nishijo H. 2014. Neuronal
1392　　　responses to face-like and facial stimuli in the monkey superior colliculus. *Front Behav Neurosci*
1393　　　**8**:1–18. doi:10.3389/fnbeh.2014.00085

1394　Niell CM, Stryker MP. 2008. Highly Selective Receptive Fields in Mouse Visual Cortex. *J Neurosci*
1395　　　**28**:7520–7536. doi:10.1523/jneurosci.0623-08.2008

1396　O'Connor DH, Peron SP, Huber D, Svoboda K. 2010. Neural activity in barrel cortex underlying
1397　　　vibrissa-based object localization in mice. *Neuron* **67**:1048–1061.
1398　　　doi:10.1016/j.neuron.2010.08.026

1399　O'Keefe J. 1976. Place units in the hippocampus of the freely moving rat. *Exp Neurol* **51**:78–109.

1400　Østergaard J, Kramer MA, Eden UT. 2018. Capturing Spike Variability in Noisy Izhikevich Neurons
1401　　　Using Point Process Generalized Linear Models. *Neural Comput* **30**:125–148.
1402　　　doi:10.1162/neco_a_01030

1403　Pachitariu M, Stringer C, Harris KD. 2018. Robustness of Spike Deconvolution for Neuronal Calcium
1404　　　Imaging. *J Neurosci* **38**:7976–7985. doi:10.1523/JNEUROSCI.3339-17.2018

1405　Paninski L. 2004. Maximum likelihood estimation of cascade point-process neural encoding models.
1406　　　*Netw Comput Neural Syst* **15**:243–262. doi:10.1088/0954-898X_15_4_002

1407　Park D, Dunlap K. 1998. Dynamic regulation of calcium influx by G-proteins, action potential
1408　　　waveform, and neuronal firing frequency. *J Neurosci* **18**:6757–66.

1409　Park E, Dvorak D, Fenton AA. 2011. Ensemble Place Codes in Hippocampus: CA1, CA3, and Dentate
1410　　　Gyrus Place Cells Have Multiple Place Fields in Large Environments. *PLoS One* **6**:e22349.
1411　　　doi:10.1371/journal.pone.0022349

1412　Park IJ, Bobkov Y V., Ache BW, Principe JC. 2013. Quantifying bursting neuron activity from calcium
1413　　　signals using blind deconvolution. *J Neurosci Methods* **218**:196–205.
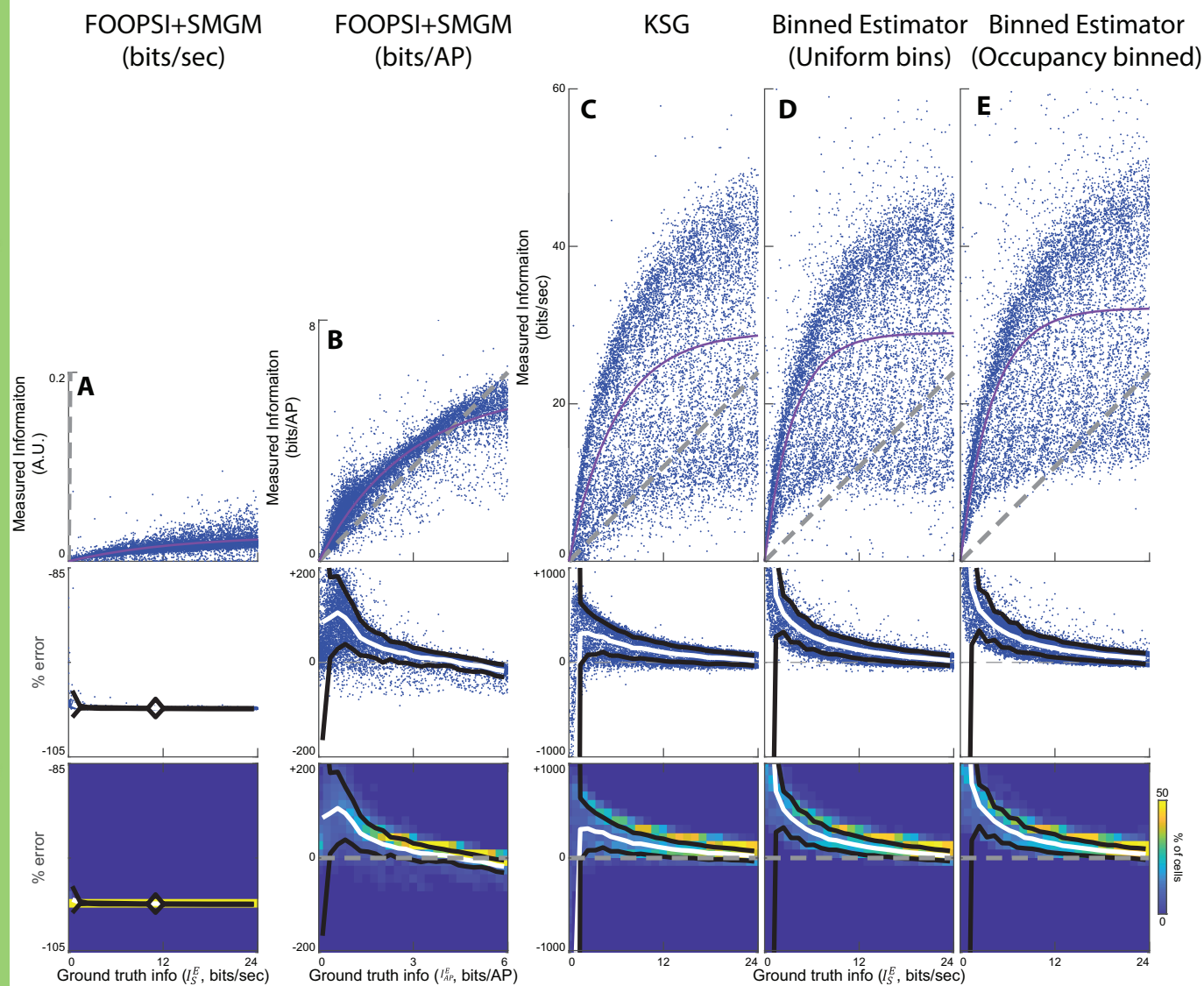1414　　　doi:10.1016/j.jneumeth.2013.05.007

43

1415   Pastalkova E, Itskov V, Amarasingham A, Buzsáki G. 2008. Internally generated cell assembly
1416   sequences in the rat hippocampus. *Science (80-)* **321**:1322–7. doi:10.1126/science.1159775

1417   Pologruto TA, Sabatini BL, Svoboda K. 2003. ScanImage: Flexible software for operating laser
1418   scanning microscopes. *Biomed Eng Online* **2**:13. doi:10.1186/1475-925X-2-13

1419   Poucet B, Sargolini F. 2013. A trace of your place. *Science (80-)* **340**:35–36.
1420   doi:10.1126/science.1237567

1421   Radvansky BA, Dombeck DA. 2018. An olfactory virtual reality system for mice. *Nat Commun* **9**:839.
1422   doi:10.1038/s41467-018-03262-4

1423   Rashid SK, Pedrosa V, Dufour MA, Moore JJ, Chavlis S, Delatorre RG, Poirazi P, Clopath C, Basu J.
1424   2020. The dendritic spatial code: branch-specific place tuning and its experience-dependent
1425   decoupling. *bioRxiv* **10**:2020.01.24.916643. doi:10.1101/2020.01.24.916643

1426   Robbe D, Buzsáki G. 2009. Alteration of theta timescale dynamics of hippocampal place cells by a
1427   cannabinoid is associated with memory impairment. *J Neurosci* **29**:12597–605.
1428   doi:10.1523/JNEUROSCI.2407-09.2009

1429   Roxin A, Brunel N, Hansel D, Mongillo G, van Vreeswijk C. 2011. On the Distribution of Firing Rates
1430   in Networks of Cortical Neurons. *J Neurosci* **31**:16217–16226. doi:10.1523/jneurosci.1677-
1431   11.2011

1432   Scholl B, Wilson DE, Fitzpatrick D. 2017. Local Order within Global Disorder: Synaptic Architecture of
1433   Visual Space. *Neuron* **96**:1127-1138.e4. doi:10.1016/j.neuron.2017.10.017

1434   Shafi M, Zhou Y, Quintana J, Chow C, Fuster J, Bodner M. 2007. Variability in neuronal activity in
1435   primate cortex during working memory tasks. *Neuroscience* **146**:1082–1108.
1436   doi:10.1016/j.neuroscience.2006.12.072

1437   Sheffield MEJ, Adoff MD, Dombeck DA. 2017. Increased Prevalence of Calcium Transients across the
1438   Dendritic Arbor during Place Field Formation. *Neuron* **96**:490-504.e5.
1439   doi:10.1016/j.neuron.2017.09.029

1440   Sheffield MEJ, Dombeck DA. 2015. Calcium transient prevalence across the dendritic arbour predicts
1441   place field properties. *Nature* **517**:200–204. doi:10.1038/nature13871

1442   Simonnet J, Brecht M. 2019. Burst Firing and Spatial Coding in Subicular Principal Cells. *J Neurosci*
1443   **39**:3651–3662. doi:10.1523/jneurosci.1656-18.2019

44

1444   Skaggs WE, McNaughton BL, Gothard KM. 1993. An Information-Theoretic Approach to Deciphering
1445   the Hippocampal Code In: Hanson SJ, Cowan JD, Giles CL, editors. Advances in Neural
1446   Information Processing Systems 5. Morgan-Kaufmann. pp. 1030–1037.

1447   Soo FS, Schwartz GW, Sadeghi K, Berry MJ. 2011. Fine Spatial Information Represented in a
1448   Population of Retinal Ganglion Cells. *J Neurosci* **31**:2145–2155. doi:10.1523/jneurosci.5129-
1449   10.2011

1450   Stackman RW, Taube JS. 1998. Firing properties of rat lateral mammillary single units: head direction,
1451   head pitch, and angular head velocity. *J Neurosci* **18**:9020–9037.

1452   Stirman JN, Smith IT, Kudenov MW, Smith SL. 2016. Wide field-of-view, multi-region, two-photon
1453   imaging of neuronal activity in the mammalian brain. *Nat Biotechnol* **34**:857–862.
1454   doi:10.1038/nbt.3594

1455   Stringer C, Pachitariu M, Steinmetz N, Carandini M, Harris KD. 2019. High-dimensional geometry of
1456   population responses in visual cortex. *Nature* **571**:361–365. doi:10.1038/s41586-019-1346-5

1457   Timme NM, Lapish C. 2018. A Tutorial for Information Theory in Neuroscience. *eneuro*
1458   **5**:ENEURO.0052-18.2018. doi:10.1523/ENEURO.0052-18.2018

1459   Treves A, Panzeri S. 1995. The Upward Bias in Measures of Information Derived from Limited Data
1460   Samples. *Neural Comput* **7**:399–407. doi:10.1162/neco.1995.7.2.399

1461   Vogelstein JT, Packer AM, Machado TA, Sippy T, Babadi B, Yuste R, Paninski L. 2010. Fast
1462   Nonnegative Deconvolution for Spike Train Inference From Population Calcium Imaging. *J*
1463   *Neurophysiol* **104**:3691–3704. doi:10.1152/jn.01073.2009

1464   Wachowiak M, Shipley MT. 2006. Coding and synaptic processing of sensory information in the
1465   glomerular layer of the olfactory bulb. *Semin Cell Dev Biol* **17**:411–423.
1466   doi:10.1016/j.semcdb.2006.04.007

1467   Wilent WB, Nitz DA. 2007. Discrete place fields of hippocampal formation interneurons. *J*
1468   *Neurophysiol* **97**:4152–4161. doi:10.1152/jn.01200.2006

1469   Yaksi E, Friedrich RW. 2006. Reconstruction of firing rate changes across neuronal populations by
1470   temporally deconvolved Ca2+ imaging. *Nat Methods* **3**:377–383. doi:10.1038/nmeth874

1471   Yartsev MM, Ulanovsky N. 2013. Representation of Three-Dimensional Space in the Hippocampus of
1472   Flying Bats. *Science (80-)* **340**:367–372. doi:10.1126/science.1235338

1473   Zhang K, Ginzburg I, McNaughton BL, Sejnowski TJ. 1998. Interpreting neuronal population activity
1474   by reconstruction: unified framework with application to hippocampal place cells. *J Neurophysiol*
1475   **79**:1017–1044.

1476   Zhou J-L, Shatskikh TN, Liu X, Holmes GL. 2007. Impaired single cell firing and long-term
1477   potentiation parallels memory impairment following recurrent seizures. *Eur J Neurosci* **25**:3667–
1478   3677. doi:10.1111/j.1460-9568.2007.05598.x

1479   Zinyuk L. 2000. Understanding hippocampal activity by using purposeful behavior: Place navigation
1480   induces place cell discharge in both task-relevant and task-irrelevant spatial reference frames. *Proc*
1481   *Natl Acad Sci* **97**:3771–3776. doi:10.1073/pnas.050576397

1482   Ziv Y, Burns LD, Cocker ED, Hamel EO, Ghosh KK, Kitch LJ, Gamal A El, Schnitzer MJ. 2013. Long-
1483   term dynamics of CA1 hippocampal place codes. *Nat Neurosci* **16**:264–266. doi:10.1038/nn.3329

1484

46

A I_{AP}^{E}=0.04 bits/AP, I_{AP}^{E}=0.7 bits/AP, I_{AP}^{E}=1.6 bits/AP, I_{AP}^{E}=1.9 bits/AP, I_{AP}^{E}=2 bits/AP

Normalized Rate ($\lambda/\bar{\lambda}$, AU)

Norm. Track Position

B Abs. Info. (I_{AP}^{E} error| (bits/AP)

Start, End

Node 3 X (m), Node 3 Y (AU)

C % Of Simulated Cells

True information (I_{AP}^{E}, bits/AP)

True Information (I_{S}^{E}, bits/sec)

D Low Info, High Info

Normalized Rate ($\lambda/\bar{\lambda}$, AU)

(mean), I_{AP}^{E}=0.04 bits/AP

I_{AP}^{E}=2 bits/AP, (mean)

Norm. Track Position

E
1) Randomly select from real behavior library

2) Use (1), $\bar{\lambda}$ and $\lambda/\bar{\lambda}$ to build instantaneous rate

Position (m), Time (sec)

Rate (Hz), Time (sec), $\bar{\lambda}$

3) Generate AP times as an inhomogenous Poisson process

4) Convolve with fit kernel and add noise to create ΔF/F response

Time (sec)

τ_{rise}, τ_{fall}, 0.2 sec, 10% ΔF/F, 50% ΔF/F, 30 sec

5) Analyze with information theoretic techniques and compare to ground truth and ΔF/F with spiking

F Track Position (m), 10 s

G Lap

H Lap, Track Position (m), Firing Rate (Hz)

I 200%, 10 s

J Lap, Mean % ΔF/F

K AP rate (λ_t, Hz), Track Position (m), Mean ΔF/F (f)

FOOPSI+SMGM (bits/sec)   FOOPSI+SMGM (bits/AP)   KSG   Binned Estimator (Uniform bins)   Binned Estimator (Occupancy binned)

F

Method	Units	Source	Mean error	Mean abs error	Mean % error	Mean abs % err	C	p exponential	saturation level	90% saturation point
SMGM bits/sec	bits ΔF/F /AP	Skaggs et al, 1993	-11.1	11.1	-96.0	96.0	0.0390	0.760	39.7	2.3e3
SMGM bits/AP	bits/AP	Skaggs et al, 1993	-0.38	0.4	-9.7	12.9	0.78	<<0.01	5.78	11.5
foopsi+SMGM bits/sec	AU	Vogelstein et al, 2010	-11.4	11.4	-99.8	99.8	1.15e-3	0.129	0.02	32.0
Foopsi+SMGM bits/ap	bits/AP	Vogelstein et al, 2010	0.3	0.6	46.3	52.7	1.02	<<0.01	5.51	6.6
KSG	bits/sec	Kraskov et al, 2004	9.9	11.9	37.9	254.8	1.64	<<0.01	29.2	13.9
Binned MI (uniform bins)	bits/sec	Timm and Lapish, 2018	12.8	14.1	285.7	292.5	1.77	<<0.01	29	8.47
Binned MI (occupancy bins)	bits/sec	Timm and Lapish, 2018	15.0	15.6	322.5	325.5	1.94	<<0.01	32.2	9.26